Discrete breathers and the anomalous decay of luminescence

2010 J. Phys. A: Math. Theor. 43 183001

(http://iopscience.iop.org/1751-8121/43/18/183001)

IOP PUBLISHING JOURNAL OF PHYSICS A: MATHEMATICAL AND THEORETICAL

J. Phys. A: Math. Theor. **43** (2010) 183001 (46pp) doi:10.1088/1751-8113/43/18/183001

TOPICAL REVIEW

Discrete breathers and the anomalous decay of luminescence

E Mihóková[1,2] **and L S Schulman**[3]

[1] Institute of Physics, Academy of Sciences of the Czech Republic, Cukrovarnická 10, 162 53 Prague 6, Czech Republic
[2] Department of Materials Science, University of Milano-Bicocca, Via Cozzi 53, 20125 Milan, Italy
[3] Physics Department, Clarkson University, Potsdam, NY 13699-5820, USA

E-mail: mihokova@fzu.cz and schulman@clarkson.edu

Received 10 December 2009
Published 16 April 2010
Online at stacks.iop.org/JPhysA/43/183001

Abstract

Some years ago an anomaly was noted in the decay of luminescence in certain doped alkali halides. The anomaly was eventually explained using a factor 1 billion (10^9) slowdown in lattice relaxation, a remarkable stretching of time scales. This slowdown was found to be caused by the creation of a '*breather*' in the neighborhood of the dopant. Discrete breathers are nondispersive classical excitations that are known to be significant in many natural systems. Broad ranging reviews of mathematical techniques and physical applications have recently appeared. In the present review we focus on the occurrence of breathers in doped alkali halides. Several more general properties of breathers have arisen from this study and these are presented as well. Among them is the study of the quantum breather, its quantization and stability, a topic less fully explored than the classical theory because it does not yield easily to numerical simulation.

PACS numbers: 63.20.Ry, 78.55.−m, 31.70.Hq, 63.20.Pw, 03.65.Sq, 31.15.xk, 05.45.−a, 78.55.Fv, 63.20.kp, 71.55.−i

(Some figures in this article are in colour only in the electronic version)

Contents

1. Introduction 2
2. Slow lattice relaxation and discrete breathers 3
   2.1. Decay anomaly in alkali halide crystals 3
   2.2. From decay anomaly to discrete breathers 9

3. Properties of discrete breathers in a diatomic lattice. KAM Tori 13
3.1. Robustness with respect to changes in the interatomic potential 14
3.2. Diatomic lattice and cation/anion mass ratio 16
3.3. Stability of classical breathers 18
3.4. Torus doubling resonances 19
4. Semiclassical quantization of discrete breathers 22
4.1. Takatsuka's frequency method 22
4.2. EBK quantization 23
4.3. KAM tori, the EBK method and stroboscopic reduction 24
4.4. Calculating the action using a stroboscopic 25
4.5. Numerical results 26
5. Stability of quantum breathers 27
5.1. Numerical diagonalization 29
5.2. Path integral approach 31
5.3. Setting up the path integral 31
5.4. Methodology 34
5.5. Localization 37
6. Breathers and noise/temperature 39
6.1. Temperature dependence of the decay anomaly 39
6.2. Models of noise 39
6.3. Non-dissipative incoherent reflection 40
7. Conclusions and remaining issues 42
Acknowledgments 43
Appendix. Simulation parameters and physical constants 43
References 44

1. Introduction

The subject of this review began with the discovery of a significant anomaly in the decay of luminescence in KBr doped with Pb [1]. The Pb was excited with ultraviolet light, and was expected to decay from two principal levels. Since one of these levels involved a highly forbidden transition, the usual pattern would have been rapid (nanosecond) exponential decay of a portion of the amplitude followed, a 'long' time later, by slow (millisecond) decay of the amplitude from the other level. Instead, there was a tremendous enhancement of the slow component decay rate during the millisecond or two following the excitation, a period when nothing of interest should have been occurring. Several straightforward explanations were considered and ultimately rejected. For example, the possibility that it was all due to unknown impurities and defects was dealt with by preparing ever more perfect crystals along with increasing dilution of the color center dopant.

It was then proposed that this millisecond long anomaly might be due to slow relaxation of the crystal. While this was a severe stretching of the time scales one ordinarily associates with crystals (nine orders of magnitude!), it did manage to explain the data, at least phenomenologically [2]. This left open the question of how relaxation could be retarded to such a degree.

The solution turned out to be the formation of *breathers*, long-lived excitations of the underlying crystal lattice that remain localized and are able to confine much of the energy

released in the KBr after the Pb is excited[4]. Such excitations exist *only* by virtue of nonlinearity in the forces between the ions of the lattice. Coming across breathers for the first time can be shocking: For the diatomic chain, one has two atoms oscillating vigorously, while an adjacent atom hardly moves at all. It would seem that elaborate choreography would be needed to avoid having the surely large forces from the second atom transmitted to the third. But then you put in a bit of noise and discover that, no, the breather is not destroyed—as your choreography intuition might have suggested—but is in fact remarkably robust. The key to understanding their stability is to think in terms of phonons. Because of the nonlinearity, the breather oscillations have frequencies either above the phonon band(s) or in the gap(s). As a result, the energy cannot be radiated away. A recent review on the subject of breathers is that of Flach and Gorbach [3], where many earlier references can be found.

In section 2 we review the experimental background, the phenomenological explanation and the basic lattice model within which the breather makes its appearance. Following that, in section 3 we review ways of describing this nonlinear excitation, for example, as a torus in phase space, essentially a KAM torus. This is also an opportunity to go into a mathematical digression describing an exotic nonlinear bifurcation that, as far as we know, was first noted in this context.

In sections 4 and 5 we turn to quantum properties. In the first of these we obtain the system's energy levels, calculated at the semiclassical level. The following section addresses the quantum stability of our breathers: after all, quantum mechanics is well known to allow classically forbidden transitions, and we demonstrate that decay of the breather, for our parameter values, is not one of them. Finally, section 6 deals with experimentally observed temperature-dependent effects and our modeling of them using noise.

2. Slow lattice relaxation and discrete breathers

2.1. Decay anomaly in alkali halide crystals

In [1] anomalous decay in the slow-emission component of isolated impurity centers in alkali halide crystals has been reported. For as long as several milliseconds one sees enhanced and non-exponential decay, going over finally to an exponential. This pattern was observed for Tl^+ and Pb^{2+} centers in various alkali halide hosts, with both fcc [4–6] and bcc [7] structure. The pressing question became, is this intrinsic or is it a consequence of crystal defects or other irregularities of the luminescent center environment. Non-intrinsic explanations were systematically excluded through improved crystal preparation, sample annealing, impurity dilution and other cautionary measures [2].

The explanation ultimately proposed [2] was that the lattice took a long time—on the order of ms—to yield to the strain caused by the Jahn–Teller deformation of the emitting center. The key feature of this slow relaxation is that the unrelaxed crystal imposes forces on the quasimolecule and sends it from the metastable level to the radiative one where it decays far more rapidly than if it had remained in the metastable level.

The emitting center is formed by the impurity ion and its nearest neighbors. For specificity, consider KBr:Pb. For the other materials and impurities the reasoning is similar (when we wish to emphasize broader applicability we may refer to the lattice as KX or KX:Pb, etc (X = Cl, Br, I)). The system is excited by a flash of UV light (408 nm). Prior to that flash, the Pb^{2+} sits in a symmetrically displaced array of the six nearest neighbor Br anions, displaced because of the large size of the Pb^{2+}. After the UV flash the $(PbBr_6)^{4-}$ system goes into an

[4] Our discussion is in terms of KBr doped with Pb. As will be evident below, this is only one of several substances in which the anomalous decay occurs.

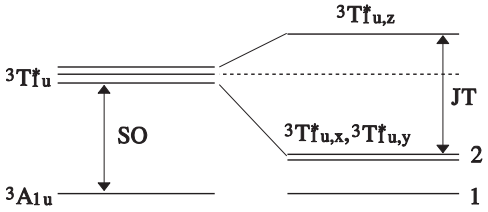

Figure 1. Energy level scheme for the relaxed excited states of the $PbBr_6^{4-}$ molecular complex with O_h symmetry in its ground state. Splitting of the levels is due to spin–orbit and JT interactions. The JT axis is parallel to the [0 0 1] direction. The asterisk on $^3T^*_{1u}$ is to remind the reader that the level is not pure triplet state, but is the state resulting from the spin–orbit mixing of $^3T_{1u}$ with an upper lying singlet $^1T_{1u}$ state. For details see [10].

excited state. Because the excited states of this quasimolecule are degenerate, according to the Jahn–Teller (JT) theorem [8, 9] it is subject to a spontaneous deformation that reduces its original (ground state) symmetry. The deformation runs along the JT axis and is highest along this axis with respect to other directions. The final splitting of excited state levels is thus a result of the spin–orbit (SO) interaction and the JT effect. The lowest excited emitting states in the potential well consist of the lower level 1, corresponding to the $^3A_{1u}$ state, and the upper level 2, corresponding to the lower doublet of the split $^3T^*_{1u}$ state; see figure 1. (This scheme is generally accepted; see, e.g., [10–12].) In both cases the $(PbBr_6)^{4-}$ system quickly relaxes to the minimum on the adiabatic potential energy surface (APES) which is a Jahn–Teller minimum with lowered symmetry relative to the original octahedral symmetry of the ground state. From this minimum it can decay radiatively (or otherwise). In the sequel, we confine attention to these two states, level 1, the 'metastable' level, with a decay time on the order of milliseconds and level 2, the 'radiative' level, with a decay time on the order of nanoseconds.

For the lower level the radiative decay is slow, giving the lattice an opportunity to relax, thereby changing the adiabatic energy levels themselves. We use the moving values of the adiabatic energy levels in the following way: for any particular lattice configuration there is some such set of states and levels (as if the lattice were frozen), and we use them as our basis vectors. The time dependence of the Hamiltonian reflects the changes in energies and interstate couplings due to changes in the lattice. We also assume that throughout this process the natural radiative decay rates, including the metastable one, can be taken to be constant (but there will be modification at higher temperatures; see below).

We concentrate on the lower level, 1, that having the slow decay. As the lattice adjusts to the distortion of the $(PbBr_6)^{4-}$ complex in its excited state (due to the Jahn–Teller effect) the entire pattern of adiabatic energy levels shifts. Of course the lower level can decay radiatively with a lifetime of several ms, as estimated in [1]. The complicating feature though is its ability to make a transition to the upper level and from there to decay quickly. This transition results from electron–lattice interactions.

The physically significant assumption is that the lattice relaxation is on the order of ms. We next show that this assumption can lead to the observed decay curves.

Assume then that a few ns after the flash the upper and lower states have a particular relative occupation. This may be the result of their being populated via a third state or having a fast phononic response kick systems from the upper to the lower state. From the perspective of our explanation of the non-exponential decay, those systems in the upper level at this point simply decay. Those in the lower level decay more slowly, but not yet with the asymptotic characteristic lifetime found in [1]. Rather (as we describe quantitatively below)

they continue to interact strongly with the upper level and amplitude leaks out of the lower level due to transitions to the upper level. This continues until lattice relaxation weakens the coupling between the levels. At this point the basic lower-level lifetime can be used to describe the exponential decay of the system. This description applies to experiments performed at low (liquid He) temperatures; at much higher temperatures there is also back transfer to the upper level, induced by phonons.

2.1.1. Zero temperature formalism. Our basis consists of the two electronic levels, which in the absence of interactions, etc, have energy difference $E(R)$ (R being a collective coordinate for the configuration of the nuclei of the $(PbBr_6)^{4-}$ complex). Without loss of generality, we can set the lower energy to zero. We also incorporate within the Hamiltonian the fact of their (radiative) instability, assigning imaginary parts to the energies. Finally we include an interaction, 'α', between the levels, which can vary with R, based on the assumption that this coupling of electronic levels is a consequence of their interaction with the neighboring atoms. The Hamiltonian reflecting these assumptions has the form

$$H = \begin{pmatrix} E(R) - \frac{\mathrm{i}}{2}\hbar\gamma_f & \alpha(R) \\ \alpha(R) & -\frac{\mathrm{i}}{2}\hbar\gamma_s \end{pmatrix}. \tag{1}$$

The quantity γ_s ('s' $\sim$ 'slow') corresponds to the slow decay, so that $\gamma_f \gg \gamma_s$ ('f' $\sim$ 'fast'). We will treat the collective coordinate R as quasiclassical, that is, not as a quantum mechanical degree of freedom, but as a parameter that finds its preferred value quickly as the lattice adjusts. This adjustment of the lattice is a reaction to the force that the local region (Pb and its immediate neighbors—the system described by our quantum formalism) exerts on the lattice. The change in the electronic state of the $PbBr_6^{4-}$ complex (due the UV illumination in the experiment) sends it to a new equilibrium intramolecular position due to the electron redistribution. This results in a distortion of the already stretched lattice (recall that the Pb is big compared to the K it replaces). So the molecular complex pushes out and the lattice pushes back. When the system reaches structural equilibrium these forces balance.

The above-mentioned adjustment of the lattice, whose configuration is also treated quasi-classically, is slow, i.e. it occurs on a ms scale. Thus, while the system is in the metastable state the lattice adjusts and the value of R is some function of time. We take that function to be

$$R(t) = R_0 + (R_\infty - R_0)(1 - e^{-\Gamma t}) \tag{2}$$

so that R_0 is the value of R taken just after the light flash. It is by assuming that $1/\Gamma$ is on the order of ms that we will produce non-exponential decay on this time scale.

When the system is fully relaxed, the splitting between the levels reaches an asymptotic value, E_f, but during the initial phases of lattice relaxation the levels should be closer, perhaps nearly degenerate. We express this change, with R, in the following way: $E(R)$ is assumed to go from some value E_0 at the earliest time, to an asymptotic value E_f. Since R is in turn a function of t, the form we assume for E is

$$E = E_0 + (E_f - E_0)(1 - e^{-\Gamma t}). \tag{3}$$

As indicated, we further assume that the strength of the coupling α varies. When the configuration of the neighbors of the Pb^{2+} ion and of the lattice for the two states are similar, the coupling of the electronic states is strong. However, as the lattice relaxes the overall states bear less and less resemblance. Our prescription is then as above

$$\alpha = \alpha_0 + (\alpha_f - \alpha_0)(1 - e^{-\Gamma t}). \tag{4}$$

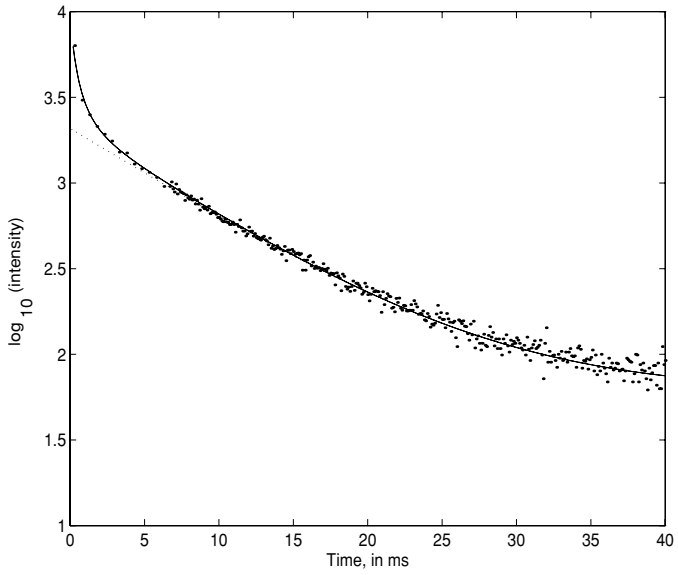

Figure 2. Decay curve ($\log_{10}$ of radiation intensity) calculated from the model. Dots represent experimental data for the decay of KBr:Pb^{2+} at liquid He temperature. The solid line is the calculated curve. For this calculation only the lower level is initially populated. The parameters (see the text for their significance) used are $\alpha_0 = 0.0075$, $\gamma_f = 4 \times 10^4$, $\gamma_s = 1/8$, $E_0 = 3$, $E_f = 45$, and $\Gamma = 0.077$, where rates are 'per ms' and energies are in meV. The dashed curve visible in the upper left is an exponential fit based on the late-arriving data and is $I = 2019 \times \exp(-t/8.06) + 61)$, where the additive constant represents the background. This curve gives an overall history. The anomaly is the discrepancy between the dashed curve and the data. It is considerable, although not prominent in this figure. Later figures (3, 4, 5) focus on this early-time domain.

The evolution of the system is calculated by assuming an initial wave function of the form $\psi(0) = \begin{pmatrix} \rho \\ \sigma \end{pmatrix}$ and evaluating the time-ordered product ($\mathcal{T}$)

$$\psi(t) = \mathcal{T} \prod_{j=1}^{j=N} \exp[-\mathrm{i}H(t_j)\delta t/\hbar]\psi(0) \tag{5}$$

with $t_j = jt/N$ and $\delta t = t/N$. This is done numerically for N sufficiently large that there is little change in H during the interval δt. From $\{\psi(t_j)\}$ the physically important quantities can be obtained. For example the radiation rate at time t_j is $[\|\psi(t_j)\|^2 - \|\psi(t_{j+1})\|^2]/\delta t$. (N.B. This does not distinguish between radiation from the upper or lower level, reflecting the experimental situation.) The slow relaxation assumption allowed successful fitting of low temperature KBr:Pb data [2] displayed in figure 2.

The model was extended to the entire collection of Pb and Tl-doped alkali halides at liquid He temperature [13]; see figures 3 and 4. The dependence of the fitting parameters on lattice and impurity allows systematic physical interpretation. As one can see from the experimental data for both Tl^+ and Pb^{2+} centers, the decay curve tends to deviate more from a single exponential as one progresses through the sequence of crystal lattices KCl→KBr→KI. The best reflection of this tendency is given by the parameter α which is the coupling between the energy levels of the excited state induced by the lattice (see equation (1)). In the sequence KCl→KBr→KI its value increases (with the same trend as the value of the halogen spin–orbit coupling parameter), indicating that the coupling between the levels becomes stronger. This

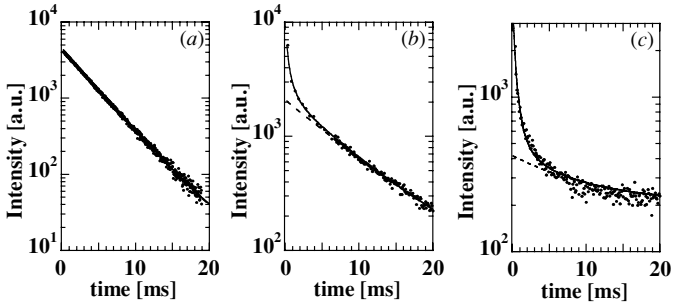

Figure 3. Decay curves calculated from the model. Marks represent experimental data for the decay of (*a*) KCl:Pb^{2+}, (*b*) KBr:Pb^{2+} and (*c*) KI:Pb^{2+} at liquid He temperature. Only the lower level is initially populated. Dashed lines represent exponential fits to the late-arriving data. In (*a*), the fit is $I = 4434 \times \exp(-t/4) + 10$; in (*b*), $I = 2019 \times \exp(-t/8.06) + 61$; in (*c*) $I = 209 \times \exp(-t/9) + 209$. The additive constant represents the background. Solid lines represent the fit to the data from our model. In (*a*) the parameters are $E_0 \geqslant 10$ meV, $\alpha_0 \leqslant 0.001$ meV, $\Gamma = 0.08$ ms^{-1}, in (*b*) $E_0 = 3$ meV, $\alpha_0 = 0.0075$ meV, $\Gamma = 0.0077$ ms^{-1}, in (*c*) $E_0 = 3$ meV, $\alpha_0 = 0.014$ meV, $\Gamma = 0.075$ ms^{-1}.

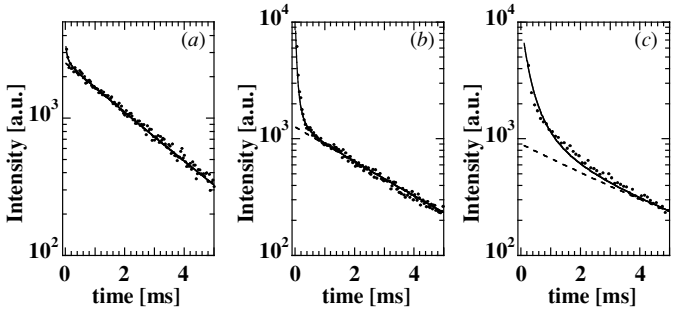

Figure 4. Decay curves calculated from the model. Marks represent experimental data for the decay of (*a*) KCl:Tl^{+}, (*b*) KBr:Tl^{+} and (*c*) KI:Tl^{+} at liquid He temperature. Only the lower level is initially populated. Dashed curves represent exponential fits to the late-arriving data: (*a*) $I = 2500 \times \exp(-t/2.37)+22.5$, (*b*) $I = 1250 \times \exp(-t/2.87)+15$, (*c*) $I = 850 \times \exp(-t/3.3)+51$. The additive constant represents the background. Solid lines represent the fit to the data from our model. In (*a*) the parameters are $E_0 = 4$ meV, $\alpha_0 = 0.005$ meV, $\Gamma = 0.7$ ms^{-1}, in (*b*) $E_0 = 3.5$ meV, $\alpha_0 = 0.025$ meV, $\Gamma = 0.6$ ms^{-1}, in (*c*) $E_0 = 5.5$ meV, $\alpha_0 = 0.035$ meV, $\Gamma = 0.2$ ms^{-1}.

is consistent with the idea that the larger and more massive lattice anions induce a stronger coupling.

On the other hand, if one looks at decay curves obtained for different centers embedded in the lattice, it is evident that the deviation from a single exponential lasts longer for the $(PbX_6)^{4-}$ center compared to the $(TlX_6)^{5-}$ center (X = Cl, Br, I). This tendency is reflected in the parameter Γ (see equation (2)). In our model Γ is connected with the speed of lattice relaxation in response to the JT distortion, and it is significantly larger for the $(TlX_6)^{5-}$ center in all crystal hosts. We suggest that the speed of a lattice response is connected to the number of lattice ions (surrounding the luminescence center) involved in the overall relaxation process. In other words, this relaxation rate depends on how far from the luminescence center the surrounding lattice is still affected by the JT distortion of a center and vice versa. The results obtained indicate that the lattice response is faster for the $(TlX_6)^{5-}$ center relative to that of the $(PbX_6)^{4-}$ center. Thus in the case of the $(PbX_6)^{4-}$ center a larger volume of the

surrounding lattice (more mass) is affected and responds. This idea is supported by two facts. First, because of the larger ionic radius (1.49 Å for Tl^+ and 1.32 Å for Pb^{2+}—see [14]) the character of the bond between the Tl^+ and the lattice anions is shifted toward a covalent type more than it is for Pb^{2+}. As a result, the response to the JT distortion is constrained to a much closer lattice environment of the $(TlX_6)^{5-}$ central quasimolecule than it is in the case of $(PbX_6)^{4-}$. Second, when Tl^+ substitutes for K^+ in the lattice, the charge distribution in the lattice remains unchanged, since they have the same charge. By contrast, Pb^{2+} substitutes for the lattice cation with an excess of a positive charge and needs a cation vacancy (v_c^-) nearby to locally compensate the charge imbalance. Nevertheless, the Pb^{2+}–v_c^- pair is an electric dipole with its own electric field. This field has long range effects and creates charge redistribution in the lattice. Therefore, it may be expected that any change in the luminescence center itself (JT distortion after an excitation) affects a much larger region of the lattice than in the Tl case.

2.1.2. Finite temperature formalism. Experimental results in [1] showed that with increasing temperature the anomalous (nonexponential) part of the slow decay gradually becomes less evident and vanishes completely around 150 K. In [15] we provide new experimental data studying the temperature dependence of the slow decay for KBr:Pb^{2+}. Moreover, we extend the theoretical model to higher temperatures.

It is convenient to rewrite H in terms of the Pauli spin matrices. In this representation

$$H = H_0 - \mathrm{i}\frac{\hbar}{2}g, \tag{6}$$

with H_0 and g real Hermitian matrices

$$H_0 = \frac{E}{2}\sigma_3 + \alpha\sigma_1 \qquad \text{and} \qquad g = \frac{1}{2}(\gamma_f + \gamma_s)\sigma_0 + \frac{1}{2}(\gamma_f - \gamma_s)\sigma_3. \tag{7}$$

In H_0 the energy has been shifted by $E/2$ relative to the form in (1), which makes no dynamical difference, and $\sigma_0 \equiv \mathbf{1}$ is the 2×2 identity matrix.

To deal with the effect of temperature we go to a density matrix formalism. The density matrix can be written in extended Bloch form [16]

$$\rho = \sum_{\alpha=0}^{3} r_\alpha \sigma_\alpha = r_0\mathbf{1} + \vec{r}\cdot\vec{\sigma}, \tag{8}$$

with $\vec{\sigma}$ the Pauli spin matrices.

To invert (8) use $r_\alpha = \frac{1}{2}\mathrm{Tr}\,\sigma_\alpha\rho$. Our Hamiltonian, (1) (or (6)), has an anti-Hermitian part, so that in place of the usual $\mathrm{i}\hbar\dot{\rho} = [H, \rho]$, the density matrix equation, at zero temperature, takes the form

$$i\hbar\dot{\rho} = H\rho - \rho H^\dagger = [H_0, \rho] - \mathrm{i}\frac{\hbar}{2}\{g, \rho\}, \tag{9}$$

with curly brackets indicating the anticommutator.

We next include the effects of thermal phonons at nonzero temperatures. Thermal coupling can induce non-radiative transitions between the levels. The change in ρ due to these transitions, when in the presence of n phonons of energy E, contributes the following term to (9)

$$\mathrm{i}\hbar\dot{\rho}_{\text{phonon}} = \mathrm{i}\hbar K \begin{pmatrix} n\rho_{22} - (n+1)\rho_{11} & -D\left(n+\frac{1}{2}\right)\rho_{12} \\ -D\left(n+\frac{1}{2}\right)\rho_{21} & -n\rho_{22} + (n+1)\rho_{11} \end{pmatrix}. \tag{10}$$

The quantity K is an asymptotic low temperature transition rate, since at sufficiently low temperature 'n' is effectively zero. It will be phenomenologically determined for our data fits.

The number D governs the decoherence. For phonon-state coupling of the spin–boson form, $D = 1$, and we adopt this value in our numerical work.

For the phonon number, n, we take the expected number of phonons of energy E to be found at temperature T. This is given by the Boltzmann factor

$$n = \frac{1}{\exp(E/kT) - 1}. \tag{11}$$

The full equation for ρ is

$$i\hbar\dot{\rho} = [H_0, \rho] - \mathrm{i}\frac{\hbar}{2}\{g, \rho\} + \mathrm{i}\hbar\dot{\rho}_{\text{phonon}}. \tag{12}$$

This is a linear equation for the four components of ρ. It is convenient to express equation (12) in terms of the components of the extended Bloch form, equation (8), by defining a column vector r with components r_0, r_1, r_2, r_3. This vector satisfies

$$\dot{r} = Wr, \tag{13}$$

with

$$W = \begin{array}{c} \begin{matrix} 0 & 1 & 2 & 3 \end{matrix} \\ \begin{pmatrix} -\gamma_0 & 0 & 0 & -\gamma_3 \\ 0 & -\gamma_0 - Kn'D & -2w & 0 \\ 0 & 2w & -\gamma_0 - Kn'D & -2a \\ -\gamma_3 - K & 0 & 2a & -\gamma_0 - 2Kn' \end{pmatrix} \end{array}. \tag{14}$$

In equation (14) we use the notation $a \equiv \alpha/\hbar$, $w \equiv E/2\hbar$, $\gamma_0 \equiv \frac{1}{2}(\gamma_f + \gamma_s)$, $\gamma_3 \equiv \frac{1}{2}(\gamma_f - \gamma_s)$, and $n' = n + \frac{1}{2}$. Our results are based on numerical integration of (13). In [15] we show the calculated fits to the experimental data in a wide temperature range, 6–110 K, and discuss the temperature dependence of the parameters of our model. Some of the data fits are shown in figure 5. The temperature dependence of the model parameters E_0, α_0 and Γ is displayed in figure 6.

To summarize, the model of slow lattice relaxation provided satisfactory fits to experimental data of various alkali halides both at zero as well as finite temperatures, allowing a unified description of the entire range of phenomena. Other explanations have also been offered[5], and they may apply in particular cases, but not for the full range of observed phenomena.

2.2. From decay anomaly to discrete breathers

Having related the decay anomaly to slow lattice relaxation, the next issue was the origin of the slowdown. By modeling the dynamics of the lattice it was found that energy could in fact be *localized* in the neighborhood of the excitation [17]. This turned out to be an experimental realization of a discrete breather. Here is the scenario. Following the UV pulse, and faster than any scale considered here, the electronic wave function, ψ, distorts. Due to the JT effect the quasimolecule is pushed hard along one axis and shrunk along the others. This creates the breather.

[5] Since the publication of [2], Ranfagni *et al* [73] have proposed an alternative explanation of the anomaly based on tunneling between emission bands. For Tl this effect may contribute, but for Pb (as the impurity), for which the anomaly is especially strong, no second emission band has been observed.

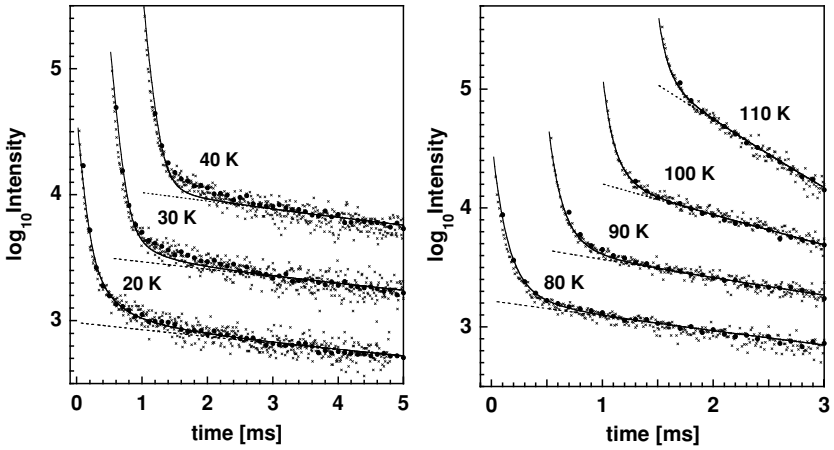

Figure 5. Decay curves of KBr:Pb^{2+} for temperatures 20 K, 30 K and 40 K (80 K, 90 K, 100 K and 110 K). Points are the experimental data. The solid curve is the fit obtained using our model with exponential lattice relaxation (see the text), with the values of the calculated curve normalized to the experimental data. The dashed curve represents an exponential fit to the late-arriving data. The axes correspond to the temperature 20 K (80 K). For better display the data for other temperatures are shifted. The respective temperatures, time shifts and log-intensity shifts are given by (30 K, 0.5, 0.4), (40 K, 1, 1), (90 K, 0.5, 0.4), (100 K, 1, 0.7) and (110 K, 1.5, 1.4).

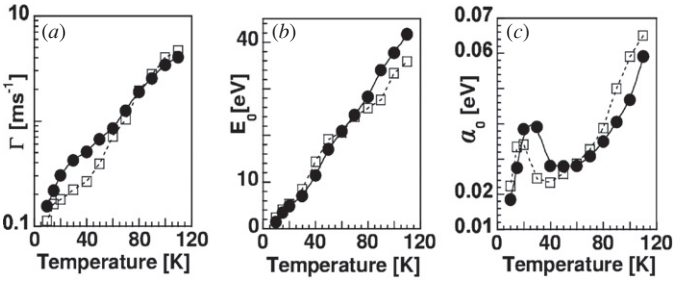

Figure 6. Temperature dependence of the parameters Γ, E_0, α_0. Solid circles represent the data obtained for the exponential lattice relaxation, while hollow squares correspond to a power law relaxation scheme (details of the latter can be found in [15]).

2.2.1. Lattice models. In the model, one focusses on a ray of atoms along the expansion axis. The first atom is subjected to a large force which it transmits to the others. Nonlinearity enters because of the large displacements. To account for the three-dimensional environment we add a potential (simulating off-chain neighbors) that tends to return each ion to its normal lattice position. We also assume that the ray of atoms opposite to those we consider is doing essentially the same thing as those we consider. As a result, the Pb atom does not have significant motion. Note that the asymmetric stresses imply lesser deformation for off-axis atoms. The interatomic potential, as a function of the displacement u is taken to be $V(u) = M\omega_0^2(u^2 + \lambda u^4)/2$. The Hamiltonian is

$$H = \sum_{n=1}^{N} \left\{ \frac{P_n^2}{2M} + \frac{r p_n^2}{2M} + V(q_n - Q_n) + V(Q_n - q_{n-1}) + \nu \left[V(Q_n) + V(q_n) \right] \right\}. \tag{15}$$

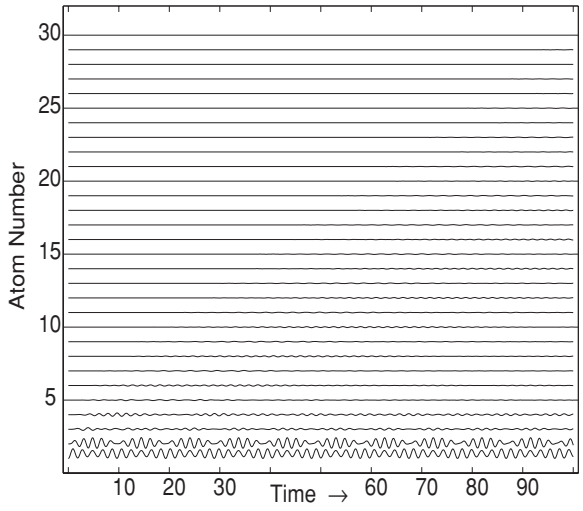

Figure 7. Position versus time. The history of confined oscillations. The lowest curve is $Q_1(t)$; above it is $q_1(t)$, etc. The parameters are $\lambda = 1$, $q_0 = 1$, $\nu = 4$, $N = 15$ (30 atoms), $r = 2$.

The notation and parameters are as follows: λ is the nonlinearity and ω_0 is a coupling whose strength will be taken from experimental data (see the appendix). ν is an effective number of neighbors and its strength determines the substrate force. Q_1 is the first atom to the right of the Pb, followed by q_1, Q_2, etc. The Q-particles have mass M, the qs, M/r. For KBr, $r \approx 2$. The impact of ψ (the distorted quasimolecule centered on the Pb) is expressed by setting (the non-dynamical) $q_0 \neq 0$. In our computations we take units such that M and ω_0 are unity.

The system was solved by numerical integration. The result was, to us, a complete surprise. Instead of the large force of the Pb causing a wave that propagated away, the energy inherent in that force remained localized in the immediate neighborhood of the Pb. The 'surprise' turned out to be a learning experience rather than a discovery, as nonlinearity-induced localization was already known under various names[6]. However, finding this phenomenon in the well-trodden field of luminescence and the Jahn–Teller effect may merit the more generous description.

Thus, under classical dynamics the energy of the extended quasi-molecule is confined to a small neighborhood of the Pb-excitation-induced-perturbation, a perturbation significant enough to make nonlinear effects important. As is evident from figure 7, the oscillation energy is substantially confined to the first two lattice ions ('Q_1' and 'q_1'). This remarkable phenomenon is insensitive to the exact parameters, including run time and number of atomic pairs N. Another illustration of confinement is the picture of the kinetic energy as a function of time and atomic number, figure 8. This too shows that the energy is substantially confined within the first two atoms of the chain. The energy deposited in the chain by the JT deformation does not propagate but becomes bound in vibrations of the first atoms of the chain, i.e. the breather. It is this lack of energy propagation that lies behind the significant slowdown in crystal relaxation and it is the origin of the decay anomaly discussed above.

We next study the frequencies of the confined vibrations. To connect to breathers this will be related to lattice phonon properties. The frequency spectrum of the first four atoms, obtained by Fast Fourier Transform (FFT) of $Q_1(t)$, $q_1(t)$, $Q_2(t)$ $q_2(t)$, is displayed in

[6] A localized excitation due to nonlinearity is sometimes known as a 'discrete breather' (DB), sometimes as an 'intrinsic localized mode' (ILM), and sometimes other names are used as well. For our application we prefer the first term, since it does not suggest translational invariance.

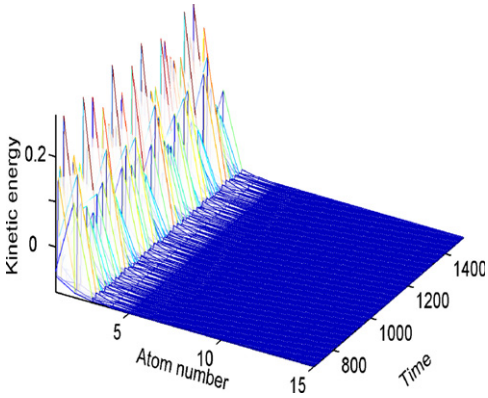

Figure 8. Kinetic energy (vertical axis) of the system as a function of time and atom number. The parameters used in the simulation are $N = 20$, $q_0 = 1$, $r = 2$, $\nu = 4$ and $\lambda = 1$.

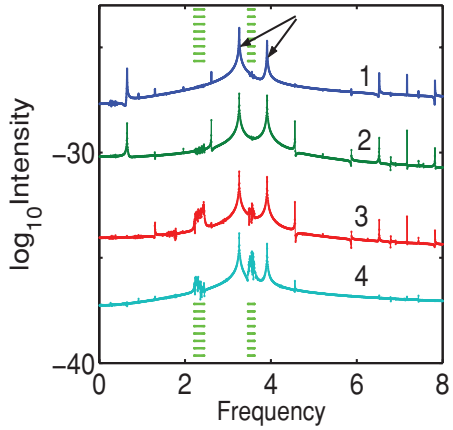

Figure 9. Fourier transforms (intensity) of the functions $(Q_1(t), q_1(t), Q_2(t), q_2(t))$ in curves 1 through 4. The curves corresponding to successive atoms are vertically shifted (downward by 4) for better display. The superimposed horizontal lines indicate where the phonon frequency bands are. Arrows point to the principal frequencies of the spectrum outside the phonon bands. All other intense frequencies are resonances or beat frequencies of these two. The parameters used in the simulation are $N = 20$, $q_0 = 1$, $r = 2$, $\nu = 4$, and $\lambda = 1$.

figure 9. Because we use finite-interval FFT, a sharp line in the true spectrum is spread, and finding maxima in the FFT spectrum is not sufficient to extract true single frequencies. In section 4.1 we show how this problem is overcome, using a method of Takatsuka [18]. The spectrum shows two dominant frequencies falling above and below the optical phonon band. These frequencies characterize the oscillations of the breather. The position of the phonon bands relative to the rest of the spectrum is marked by a sequence of horizontal lines. It is important, with respect to the localization of the excitation, that the breather frequencies do indeed fall outside the phonon bands. Note too that because our model imposes a holding (or substrate) force to simulate atoms not included in the model, important phonon modes are missing. In particular, low frequency modes, allowed in a true crystal, do not occur in the model. As a consequence, the acoustic phonon band does not start from zero frequency.

Besides the extreme spatial localization, another property of our confinement curves—perhaps *the* characteristic soliton feature in the Fermi–Pasta–Ulam (FPU) study—is the failure

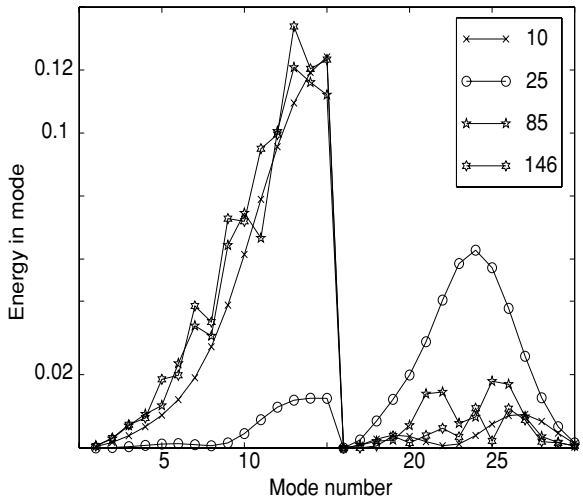

Figure 10. Energy per normal mode at various times. Parameters are $\lambda = 1$, $q_0 = 1$, $\nu = 4$, $N = 15$, $r = 2$.

of energy to disperse among the normal modes. Figure 10 shows energy dispersal for various times. Unlike FPU, our initial conditions preclude concentration in one mode. Nevertheless, it is clear that while energy can shift from mode to mode (cf time-25 in the figure), it tends to return repeatedly. Note that because of nonlinearity the energy in each mode need not be conserved.

3. Properties of discrete breathers in a diatomic lattice. KAM Tori

Our focus will be on the existence of a second breather frequency (in contrast to the monatomic lattice), since there is already an extensive literature on the monatomic classical case. An important tool for visualization in this context is the KAM torus. This is a structure in phase space, and is named for the mathematicians (Kolmogorov, Arnold, Moser) who showed its presence for small nonlinearity [19, 20]. Although the Jahn–Teller-induced dynamics is strongly nonlinear, the toroidal phase space structure does appear and we refer to it as a KAM torus. For our systems, the torus is two-dimensional even when substantially more than the first two atoms on the chain are oscillating. Thus the dimensionality is not related to the number of significantly participating atoms and is a reflection of the *di*atomic nature of the solid. A stroboscopic analysis reveals loop subsets of the torus (easily understandable in an action-angle context). These loops play a vital role in the quantization of breathers, as described in section 4, and the two-dimensionality makes possible the calculation of quantum levels in these systems.

In figure 11 we show a projection of the KAM torus which is the classical phase space orbit of the breather. Superimposed is a pair of loops, which result from a stroboscopic image of the torus. As will be developed in section 4, the ability to produce such a figure takes advantage of the existence of a transformation (à la KAM), albeit an unknown one, to action-angle variables such that the Hamiltonian is a function of the action variables only. With $\{J_1, \theta_1, \ldots\}$ the variables, the torus is given by the equations $\theta_k = \omega_k t + \theta_{k0}$ (with $\omega_k = \partial H/\partial J_k$), $k = 1, \ldots, N$ and N the number of coordinate degrees of freedom of the system. If one knows one of the ω_k's, then by viewing the full orbit only at multiples of $2\pi/\omega_k$

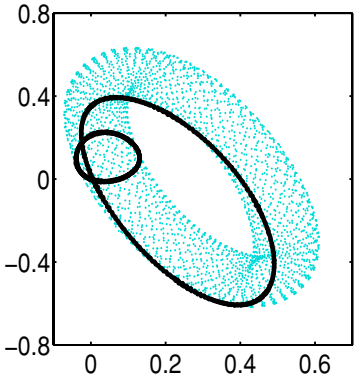

Figure 11. The KAM torus, projected on a plane within the four-dimensional space $\{Q_1, P_1, q_1, p_1\}$. The figure contains 100 000 points, with 100 points taken per system time unit. The abscissa is position and the ordinate momentum in the units described in the appendix. Loops in the torus represent projections on the Q_1–P_1 and q_1–p_1 planes of the stroboscopically viewed KAM torus, substantiating the assertion that the torus is two-dimensional (only has two significant nonzero radii). The parameters used in the simulation are $N = 20, q_0 = 1, r = 2, \nu = 4$, and $\lambda = 1$.

a torus of one lower dimension is generated. These are the loops of figure 11, one for each of the dominant frequencies. The fact that these are clean, one-dimensional loops implies that the KAM torus for our simulations is only a two-dimensional structure[7]. This is of course consistent with the presence of only two dominant frequencies outside the phonon bands in the frequency spectrum although there is no *requirement* that only two frequencies appear. The original momenta and positions are nonlinear functions of the action-angle variables, so that in analyzing Q_1 and other functions, one can certainly obtain beats and multiples of the 'true' ω's.

3.1. Robustness with respect to changes in the interatomic potential

The appearance of breathers in the dynamics of the Hamiltonian (15) is not restricted to the potential $V(u) = M\omega_0^2(u^2 + \lambda u^4)/2$, and is far more general. This is shown in [21] for a variety of interatomic potentials and is especially evident using KAM tori. The degree of localization varies with the potential, but for strong enough nonlinearity it is always present.

There are a number of potentials that are popularly used for the description of interatomic forces. We mostly use the notation of [22], an article that also addresses nonlinearity-induced localization[8].

Polynomial interatomic potential

$$V_P(x) = M\omega_0^2\left[\frac{1}{2}x^2 + \frac{\kappa}{3}x^3 + \frac{\lambda}{2}x^4\right] \tag{16}$$

where M and ω_0 are taken to be 1 in our work.

[7] In principle, the loop we see could be the projection from a higher dimensional structure. This would be a (non-generic) coincidence, but coincidences do happen. Nevertheless, that is not occurring here. In our investigations we simultaneously viewed more than one projection of the torus, and when there was a one-dimensional loop in one plane, there was a one-dimensional loop in the others. This can be seen in figure 12(*d*), where we do show more than one plane.

[8] Kiselev *et al* [22] discusses 'intrinsic' localized modes, working in a translationally invariant context, which is not the case in our situation.

Morse interatomic potential

$$V_M(x) = P(\mathrm{e}^{-ax} - 1)^2. \tag{17}$$

Born–Mayer–Coulomb interatomic potential

$$V_{BMC}(x) = \frac{\alpha_M q^2}{d^2}\left[-\frac{d^2}{x+d} + \rho\,\mathrm{e}^{-x/\rho} + d - \rho\right] \tag{18}$$

where α_M is the Madelung constant, q is the effective charge, d is the distance between adjacent particles and ρ describes the repulsion between atoms.

Others: The Toda potential ($V(x) = (a/b)\,\mathrm{e}^{-bx} + ax - a/b$) and Lennard–Jones potential ($V(x) = \epsilon\{[d/(x+d)]^{12} - 2[d/(x+d)]^6 + 1\}$) are also often used, but we did not examine their breather-formation properties.

We performed lattice dynamics simulations using the potentials of equations (16)–(18). For simulations of chain dynamics with Morse and Born–Mayer–Coulomb (BMC) interatomic potentials, equations (17) and (18), the parameters entering potentials were chosen in such a way that the potentials are somewhat 'softer' than the polynomial potential. Nevertheless, the results in all cases provide substantial kinetic energy confinement extended to the region of the first five to six atoms of the chain. Frequency spectra as in figure 12(*b*) appear to have several dominant frequencies, but there still turn out to be only two truly independent frequencies, corresponding to two degrees of freedom of the system represented by two-dimensional KAM tori in multidimensional phase space (figures 12(*c*) and (*d*)).

The two-dimensional Morse and BMC tori eliminate one argument that might have seemed reasonable to justify the low KAM torus dimension in the other cases. For the quartic polynomial potential, for most of the parameter values we analyzed in detail, hardly more than two atoms were substantially involved. Atoms number 3 and 4 do have a small percentage of the energy, but you might have argued that with most of the energy localized on only two coordinates the KAM torus would be similarly confined in phase space. But for BMC and Morse, four or five atoms move appreciably.

Determination of the dominant frequencies of the breather with high accuracy (5 digits) is the most important issue for establishing the number of degrees of freedom of the breather, or the dimension of the KAM torus. For the BMC potential we needed to apply a special 'cleaning mechanism' to the frequency spectrum. Two problems were at work. First there is a finite size effect: although most energy (due to nonzero q_0) remains in the breather, a small amount is typically radiated away. When this bounces off the far boundary (usually at the 40th atom in our simulations) it will return to disturb the breather. Second, and more fundamental, is that quite a few additional frequencies show up in the BMC spectrum. As it later turned out this was *not* because the dimension of the torus was greater than 2, but (we believe) is the result of the transformation from action-angle variables being more nonlinear than for the other cases. The first problem was dealt with by putting a damping force on the last atoms of the chain so that the energy that reached the boundary was dissipated and did not reflect. This does clean up the spectrum a bit. As indicated, our determination of frequency used a method of Takatsuka [18], see also section 4.1 (as implemented in [23]). The BMC spectrum was more complicated yet, with a background of what appear to be many frequencies. We dealt with this by using the single frequency method of [18] and then using properties of classical mechanics to improve upon it. A stroboscopic view with the raw initially derived frequency gives a rather fragmented image, but by searching nearby frequency values lovely loops emerged, and in fact only *two* of them (for the two principal raw frequencies), cf figures 12(*c*) and (*d*). In [23]

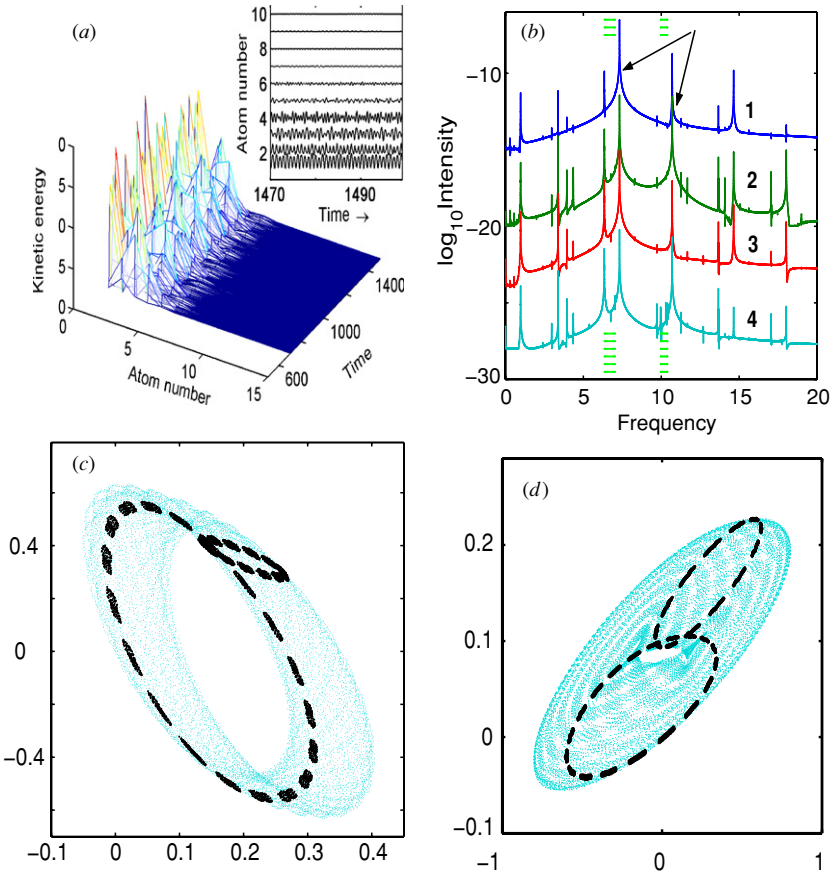

Figure 12. Born–Mayer–Coulomb potential. (*a*), (*b*) and (*c*) as in figure 1. (*d*) The KAM torus projected on a different plane. Parameters used in the simulation: $N = 20, q_0 = 1, r = 2, \nu = 4, \alpha_M q^2/d = 10, \rho = 0.3$ and $d = 3.3$.

the sharpness of the strobed loops originally served as a check on frequency; in the present context it becomes a yet finer tool for ascertaining the true underlying classical values.

A study of the chain dynamics with the foregoing collection of interatomic potentials confirms that the confinement phenomenon, which in our situation means breather formation, is not a property of a specific choice of interatomic potential. Rather it is a robust feature of the dynamics.

3.2. Diatomic lattice and cation/anion mass ratio

Other physically significant aspects of the breather were checked. Physical observations showed systematic behavior of the anomaly when the host lattice is changed. Namely for potassium halides doped either with Tl^+ or Pb^{2+} the anomaly grows (the nonexponential part of the decay is steeper and/or survives to longer times) with increasing size and mass of the lattice anion. This occurs in the sequence of lattices KCl→KBr→KI (cf figures 3 and 4). Experimental results with Pb^{2+}-doped NaBr and RbBr crystals [24] show that similar behavior is observed in the sequence of lattices RbBr→KBr→NaBr where the lattice cation is

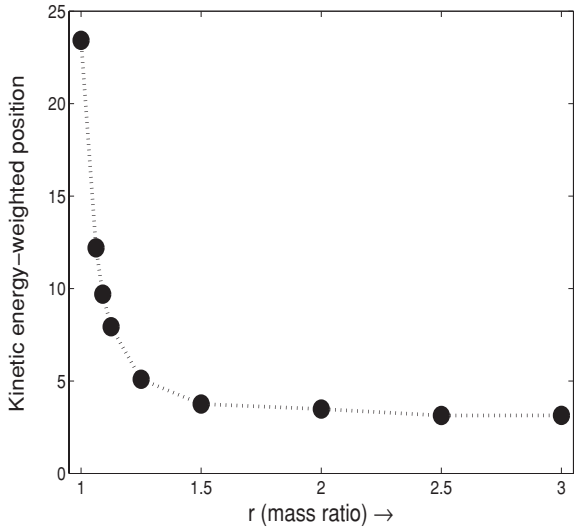

Figure 13. Kinetic energy-weighted position (in atomic spacing units) as a function of the anion-cation mass ratio. For details see the text. The parameters used in the simulation are $N = 20$, $q_0 = 0.5$, $\nu = 4$, and $\lambda = 0.25$.

successively made smaller and lighter. Therefore, a quantity that certainly affects the character of the decay anomaly is r, the ratio of the mass of the lattice anion to that of the lattice cation. Experimental results suggest that alkali halides for which the anion-cation mass ratio is close to one have little or no anomaly in their luminescence decay; as the ratio grows the anomaly increases. Breather formation exhibits a similar effect: for moderate nonlinearity, as this ratio approaches unity the breather gets more and more delocalized, and for appropriate parameters disappears completely. (Of course for sufficiently large nonlinearity there will be a breather: this is just the monatomic case.) To study the breather as a function of the anion-cation mass ratio we used our standard polynomial potential. We performed lattice-dynamics simulations changing the atomic mass ratio entering the chain model. It turns that different mass ratios can be more or less favorable for forming the breather. The simulations were made for a chain of 40 atoms. As a measure of the degree of confinement of the energy to the region of the impurity, we calculated a kinetic energy-weighted position. That is, let k be the atom number, $k = 1$ for the immediate neighbor of the impurity, and counting outward. Let $w_{KE}(k)$ be the average kinetic energy of the kth atom. Then

$$k_{KE} \equiv \langle k \rangle = \frac{\sum_k k w_{KE}}{\sum_k w_{KE}}. \tag{19}$$

The smaller this quantity, the more the energy concentrated in the breather, and therefore the bigger the expected decay anomaly. We chose this measure of confinement because of the usefulness of the kinetic energy plot (see figure 8) for immediate recognition of the confinement phenomenon. The result of a systematic study of k_{KE} as a function of r is shown in figure 13. Note that for the parameters used, as $r \to 1$, there is a kind of phase transition, namely $k_{KE} \to \infty$, where '∞' for this finite lattice means halfway to the boundary, i.e. a delocalized excitation.

Additional support for the breather mechanism comes from studies of the *same* substance, undergoing JT deformation along *different* axes. When the JT axis does not provide a chain

of nearest neighbors, there is essentially no anomaly. It is known that the quasimolecule associated with an isolated impurity and its nearest neighbors in alkali halide crystals under excitation undergoes JT distortion either along tetragonal or trigonal axes. Some substances show two emission bands: one is called the A_T emission and is related to a tetragonal distortion, the other, A_X emission, is related to a trigonal distortion. With respect to potential breather formation these distortions are quite different. In one case (A_T, tetragonal) there is a line of nearest-neighbor atoms, allowing the physical picture described in our model. In the other (A_X, trigonal) direction there is no chain of nearest neighbor atoms. Experimentally we have observed both emissions for KBr:Tl and NaBr:Pb crystals. In both crystals the anomaly was observed only for the slow component of the A_T emission, while A_X emission decay showed no anomaly. Decay anomalies either reported above or cited have *always* been associated with the A_T band.

3.3. Stability of classical breathers

Discrete breathers in one-dimensional *monatomic* lattices are known to exist [25, 26]. However, one expects that in a diatomic lattice the presence of two frequencies at which significant oscillation takes place could cause resonances and destroy the breather. (One breather frequency is above the optical phonon spectrum of the lattice, while the other is in the gap between the acoustical and optical phonon bands.) In [27] we provided evidence for the survival of breathers on the scale necessary for the explanation of the experimental data, namely 10^9 natural lattice time units, more than 10^8 breather oscillations.

Finding a good measure of breather stability is not straightforward. For example, the total energy in any finite subset of atoms will vary. Amplitudes are similarly difficult to get information from (cf section 4.1). Radiated energy (if there is any) is difficult to distinguish from either the exponential dropoff (with distance) in breather excitation or from residual excitation present even after we have done our best to create a pure breather. The ideal quantity would be the action, the variable 'J' that is constant in the (unknown) action-angle variables that solve the problem. This is not an easily computable quantity, and we have instead taken a closely related quantity, the frequency, $\omega = \partial H/\partial J$, as a surrogate for J. As we now show, these frequencies, associated with the breather, are extremely stable.

The system is begun at rest (all q's, $\dot{q}$'s, Q's and $\dot{Q}$'s zero) with the non-zero value of q_0 (the 'push' from the Jahn–Teller distortion) forcing the system into motion. For a preparatory period, typically 1000 or 1500 time units, the far end of the chain is dissipative. Thus, a breather is formed with any non-breather excitation radiated away and absorbed. After this, the profile, energy as a function of atom number, declines approximately exponentially. In addition, there are certain computational tricks, described in section 6.3, to avoid coherent reflections off the far end of the chain. The amount of energy remaining after the radiation is a function of the parameters. For fixed ν and λ, as q_0 increases, this energy increases, although there was no evidence of sudden changes.

Once the dissipation is turned off the system evolves under pure Hamiltonian dynamics for (typically) 5000 time units. This interval is broken into smaller times, from 200 to 1000 time units, and the dominant frequencies measured in a moving window with this width. Evaluation of the frequency uses the method described in section 4.1. Further details on the application of this method to our system can be found in [23].

As is evident from figure 14 and its caption, the frequencies hardly change at all. A linear fit gave slopes consistent with zero. We mention that in cases where the breather *is* decaying for one reason or another (e.g. when there is noise present, as in our finite-temperature studies, section 6), there is a clear response in the frequency dependence.

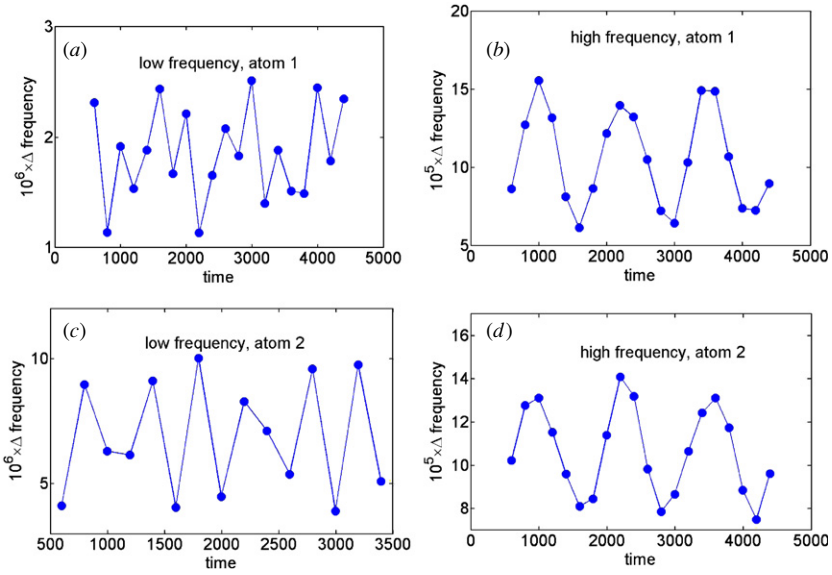

Figure 14. Breather frequencies for the first two atoms in a moving window of width 900 time units, for a run of 5000 time units. In each case a fixed frequency (given below), f, is subtracted from the values in the graph. Note that the frequencies cluster in an extremely narrow range. We estimated their change in time with a linear fit, which gave us rates of change that were consistent with zero. Specifically we found that (slope, standard deviation) for the 4 cases graphed is (*a*) $(4.5657 \times 10^{-11}, 8.4086 \times 10^{-11})$, (*b*) $(-4.8344 \times 10^{-9}, 6.0324 \times 10^{-9})$, (*c*) $(5.3209 \times 10^{-11}, 9.8383 \times 10^{-11})$, (*d*) $(-3.97 \times 10^{-9}, 3.9778 \times 10^{-9})$. (For graph (*a*), the frequency displacement is $f_a = 1.927\,53$; similarly, $f_b = 2.8129$, $f_c = 1.799\,14$, $f_d = 2.8129$.)

In an effort to understand the extreme stability against radiation, we checked whether combinations (sums of multiples with both positive and negative integer coefficients) of breather frequencies landed in the phonon bands. It is such combinations that would appear in nonlinear terms acting on the phonon modes, hence inducing radiation and decay of the breather. It turned out that combinations of the smallest higher harmonics that land in the optical band have intensities down by about 7 powers of 10. It is thus completely reasonable that their effect is suppressed at the level that we found.

Returning to the physical demands of our model, we conclude from these data that the frequency is unchanging on a time scale of 10^{-9} units. This implies that the mechanism responsible for the anomaly in luminescence decay is not affected by the in-principle problem associated with multiple frequencies in the diatomic lattice. Moreover, we feel that it is remarkable that conclusions can be drawn on system behavior that deal with times that are five or more orders of magnitude longer than the actual computer runs.

3.4. Torus doubling resonances

Of further interest with respect to the general understanding of nonlinear phenomena is the behavior of the system in the neighborhood of a resonance. One might have thought this to be particularly dangerous to the survival of the breather, but what actually occurs is a kind of bifurcation, which, as far as we know, has not previously been observed. Below the resonance (in the control parameter q_0), the system lives on a torus in phase space. As the critical region is approached there is a period doubling, just as for an ordinary orbit, but with the entire torus

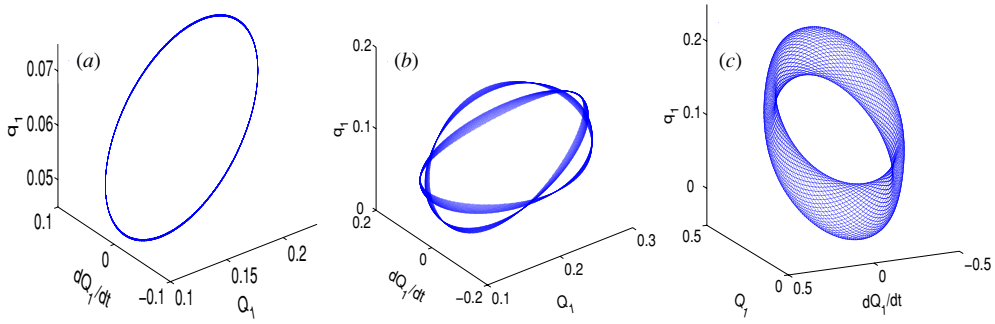

Figure 15. Phase space structures for $q_0 = 0.4$, 0.498 25 and 0.59.

doubled. Once the resonance has passed (as a function of q_0), the system goes back to the usual torus. Now one could certainly see a torus bifurcation if a system with a loop-orbit bifurcation had attached to it a non-interacting or perhaps weakly interacting oscillator. But in this case both dimensions of the torus are inextricably intertwined and one could not reduce the torus to a loop while maintaining the bifurcation.

Phase space structures for nonlinear systems are famously complex [28], with the concepts of bifurcation and period doubling playing an important role. As we now show, both of these occur in our system, but because of the dimension of the structure we cannot use the most direct kind of Poincaré section to illustrate the phenomena. On the other hand, the dimension is not so high that our bifurcation should be rare.

We will refer to the phenomenon as *torus doubling*, since the phase space structure consists of a torus that passes through itself, at least when thought of as a subset of 3-space. We have established, however, that on a full loop of the doubled-torus, orientation is preserved.

For the present discussion, the parameters of the Hamiltonian (15), are fixed. (We take $\lambda = 1$ and $\nu = 1$, while M and ω_0 are 1 by virtue of the units.) As indicated, the control parameter is q_0, the force on the first atom due to the Jahn–Teller effect.

To give an overview, in figure 15 we show phase space structures for various values of q_0. What is illustrated is the points $(Q_1(t), \dot{Q}_1(t), q_1(t)) \subset \mathbb{R}^3$ for $t = n\Delta t, n = 1, 2, \ldots, N, N = T/\Delta t$ with $T \sim 5000$ and Δt usually taken to be 0.1. For small q_0 one gets a thin torus, while for large q_0 one also gets a torus, but with both radii large. In the intermediate region, near $q_0 = 0.5$, there is a period doubling, with the center of the torus forming a curve approximately twice the length of the unsplit loop.

A detailed investigation reveals the following.

- The dominant frequency for $q_0 \lesssim 0.47$ is the breather frequency in the gap between the acoustic and optical phonons denoted ω_ℓ (for 'low'). The other breather frequency, that above the optical band, ω_h ('high'), has smaller, but nonzero amplitude (cf figure 16).
- In the neighborhood (with respect to q_0) of the torus doubling, the ratio of ω_h to ω_ℓ is close to 3-to-2. This implies that the half-frequency, which is associated with period doubling, is increasingly excited by nonlinear terms in the equation of motion. As a resonance, this is the lowest possible order (1–1), with $\omega_h - \omega_\ell \sim \omega_{pd}$, where $\omega_{pd} = \omega_\ell/2$ is the period-doubling frequency (cf figure 16).
- Fourier transforms of the positions of the first four atoms confirm the excitation of the period doubling frequency; interestingly, there is greater amplitude for the half-frequency $(\omega_\ell/2)$ in the second atom than in the first (cf figure 16).

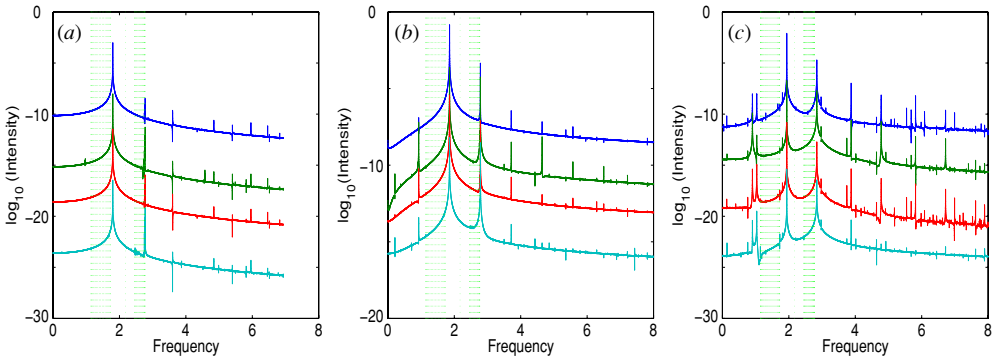

Figure 16. Frequency spectra of the first 4 atoms for $q_0 = 0.4, 0.498\,25$ and 0.59 ((*a*), (*b*), and (*c*), respectively). (Atom 2's spectrum is displaced by 4 units below that of atom 1, etc.) The horizontal green bands traversing the figures vertically represent the phonon bands (acoustic and optical).

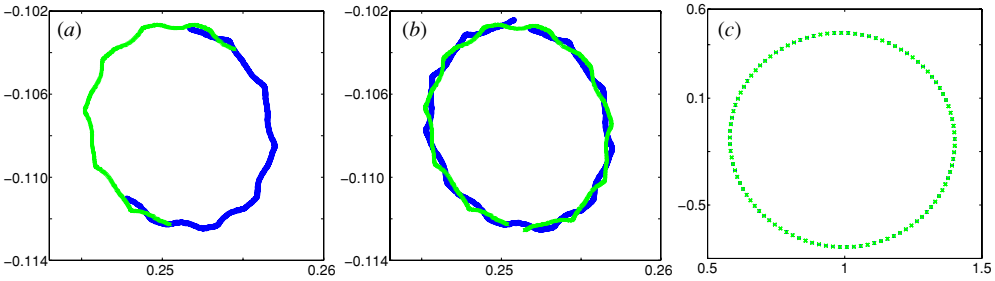

Figure 17. Strobing at the period doubled frequency ($\omega_\ell/2$). The images (*a*), (*b*) are for the dynamical simulation, with runs of 3000 and 5000 time units, respectively. Points are labeled according to whether they enter on odd or even numbered strobe images (one set consists of (darker) blue circles, the other in (lighter) green x's (*c*)). For the shorter interval the torus has not filled out and the two portions have not quite met. For 5000 time units the torus has nearly filled out completely and it is clear that there are two separate portions. The image c is what one gets for the Lissajous figure, a combination of sines and cosines with frequencies 1.01 and 1.5, close to the 3–2 ratio.

- The double loop is not knotted.
- Close to exact matching of the frequency ratio, one requires very long computer runs to see the torus fill out. For shorter times one gets a closed ribbon-like structure. By checking the orientation of lines on cross sections of the ribbon, we found that the orientation does not change, i.e. it is a cylinder and not a Möbius strip.
- For longer runs, the portion of the loop formed in the second half of the doubled period nearly overlaps with the first. By averaging over successive cross sections however one can see that this averaged quantity behaves like the doubled orbit in lower dimensional period doubling orbits (e.g. for the Duffing equation, [29], figures 11–7, or the Rössler equation, [30], figure 3).
- It is important to distinguish the doubled torus from a 3–2 ratio Lissajous figure. With a ratio close to (but not exactly) 3–2 and for runs of finite length, such a figure can indeed resemble figure 15(b). Nevertheless a sharp distinction can be drawn by stroboscopic cross sections with varied time intervals (see figure 17).

- The same phenomenon occurs for $\nu = 0.75$ for q_0 near 0.59, indicating that torus doubling is generic.
- As remarked above, the period doubling of our torus is not simply the doubling of a one-dimensional orbit, fattened by an extra oscillator. By adjusting additional control parameters one can indeed suppress one or the other breather frequency[9]. However, the essence of this bifurcation is a 3–2 resonance involving *both* these modes, depending thereby on the nonlinear coupling. Hence, the phenomenon studied here intrinsically depends on the full torus structure.

4. Semiclassical quantization of discrete breathers

To complete a physical theory of breathers one must quantize this excitation. The computation of breather energy levels was accomplished in [23] and is described in the present section. The quantum decay theory is treated in section 5.

Although for physically relevant breathers there are only two degrees of freedom to quantize, they are embedded in far more: the breathers are collective nonlinear modes. While the involvement of distant atoms is small it must be taken into account, despite the small oscillation amplitudes. Fortunately, the experimental regime is one in which semiclassical methods should be effective. Since the motion is regular, EBK quantization (Einstein–Brillouin–Keller) [31–33] can be applied. Approaches related to EBK have been used in a variety of applications [34–43]. The key to our implementation of EBK quantization is a stroboscopic view of the KAM torus. If desired, the method provides wave functions. We also present a derivation of EBK that allows a generalization of the form contemplated in [44, 45].

4.1. Takatsuka's frequency method

In [18], Takatsuka describes a method for obtaining precise frequency information from a time series, based on the FFT. This method gives remarkable precision, well beyond a naive uncertainty principle estimate. What allows this improvement is the assumption that there is a single dominant frequency. We mention a second frequency determination method, due to Laskar [46], a version of which was used in an attempt to determine amplitudes.

Assume that the underlying signal has the form

$$\phi(t) = A\,\mathrm{e}^{\mathrm{i}\omega t}. \tag{20}$$

The data consist of ϕ evaluated at N points, $t = j\Delta t$, $j = 1, \ldots, N$ and $\Delta t = T/N$, with T the total time interval. Using the Fourier transform conventions of MATLAB™ yields

$$\begin{aligned} X(k) &= \sum_{j=1}^{N} \phi(j\Delta t)\,\mathrm{e}^{-\frac{2\pi\mathrm{i}}{N}(j-1)(k-1)} \\ &= \sum_{j=1}^{N} A \exp\left(ij\left[\omega\Delta t - \frac{2\pi}{N}(k-1)\right] + \frac{2\pi\mathrm{i}}{N}(k-1)\right). \end{aligned} \tag{21}$$

Introduce the notation

$$r \equiv \exp\left[\mathrm{i}\left(\omega\Delta t - \frac{2\pi}{N}(k-1)\right)\right], \qquad z \equiv \mathrm{e}^{\frac{2\pi\mathrm{i}}{N}(k-1)} r(1-\mathrm{e}^{\mathrm{i}\omega T}) = \mathrm{e}^{\mathrm{i}\omega\Delta t}(1-\mathrm{e}^{\mathrm{i}\omega T}). \tag{22}$$

[9] This was carried out in [23], where the action was systematically calculated as a function of displacement of *both* first and second atoms.

Note that z does not depend on k. Then

$$\frac{X(k)}{A} = \left(\sum_{j=1}^{N} r^j\right) \exp\left(\frac{2\pi \mathrm{i}}{N}(k-1)\right) = z\frac{1}{1-r}. \tag{23}$$

Let k_0 be such that $k_0 - 1 < \frac{N}{2\pi}\omega\Delta t \leqslant k_0$, and examine the ratio

$$R_k \equiv \frac{X(k+1)}{X(k)} = \frac{1-r_k}{1-r_{k+1}} = \frac{1-\exp\left(\mathrm{i}\omega\Delta t - \frac{2\pi \mathrm{i}}{N}(k-1)\right)}{1-\exp\left(\mathrm{i}\omega\Delta t - \frac{2\pi \mathrm{i}}{N}k\right)}. \tag{24}$$

Define x, $0 \leqslant x < 1$, through the equation $\omega\Delta t = \frac{2\pi}{N}(k_0 - x)$. For small $\ell \equiv k - k_0$, since $2\pi/N$ is small,

$$R_k \approx \frac{\omega\Delta t - \frac{2\pi}{N}(k-1)}{\omega\Delta t - \frac{2\pi}{N}k} = \frac{\ell + x - 1}{\ell + x}. \tag{25}$$

What makes Takatsuka's method work is the fact that *this quantity is positive except for* $\ell = 0$, allowing an easy numerical search for k_0. We thus identify k_0 by the condition $R_k < 0$. For this value

$$R_{k_0} = \frac{x-1}{x} \quad \Rightarrow \quad x = \frac{1}{1-R_{k_0}}. \tag{26}$$

This gives the estimate for ω,

$$\omega = \frac{2\pi}{N}\frac{1}{\Delta t}(k_0 - x) = \frac{2\pi}{T}\left(k_0 - \frac{1}{1-R_{k_0}}\right). \tag{27}$$

For the pure signal $\phi(t)$ one can obtain the magnitude of the amplitude A as well. By straightforward steps one obtains

$$|A| = (2\pi/N|z|)|X_{k_0+1}||X_{k_0}|/|X_{k_0} - X_{k_0+1}|. \tag{28}$$

In practice, it turns out that even if one does not have a purely monochromatic signal, the frequency estimate remains excellent. However, the amplitude estimate is less robust and our results do not depend on it. The frequency estimate, equation (27), though has been found accurate far beyond $\mathrm{O}(1/N)$, as we have checked numerically by feeding in pure and mixed artificial signals. An analog of the Laskar method [46] was used for amplitudes, and was slightly more reliable than equation (28), but we have not used amplitude estimates for any of our conclusions.

The frequency estimates of Takatsuka [18] are essential for the stroboscopic method that we use for evaluating the classical action.

4.2. EBK quantization

EBK quantization is a multidimensional form of Bohr–Sommerfeld quantization and dates to Einstein's prescient 1917 article [31]. Brillouin [32] and Keller [33] brought the method to its present form (the latter introducing phases often attributed to Maslov, and which may predate Keller as well). In this article we give a different derivation, following [23]. It is shown there that the imprecision due to operator-ordering ambiguities can lead to $\mathrm{O}(\hbar^2)$ changes in the quantized energy values—but not more than that.

The system we quantize is not chaotic, so there exist classical action-angle variables $(J_1, \theta_1, \ldots, J_N, \theta_N)$, with $H = H(J_1, \ldots, J_N)$, reached by canonical transformation from the original p s and qs. This mapping is not known explicitly, but it gives the $\{J, \theta\}$ as functions of the original variables. Thus, quantizing in (J, θ) will give a spectrum within

$\hbar^2$ of the true spectrum. Quantization is accomplished by requiring $[J_\ell, \theta_{\ell'}] = -\mathrm{i}\hbar\delta_{\ell\ell'}$, from which follows $J_\ell = (\hbar/i)\partial/\partial\theta_\ell$. Eigenfunctions are therefore of the form $\exp(\mathrm{i}k_\ell\theta_\ell)$. There arises the problem of boundary conditions. From general principles, an advance of 2π can only change the wave function by a phase factor, $\exp(\mathrm{i}2\pi\mu)$, for real μ. Therefore, for each degree of freedom,

$$\psi(\theta_\ell + 2\pi) = \exp(\mathrm{i}2\pi\mu_\ell)\psi(\theta_\ell) \Rightarrow k_\ell = n_\ell + \mu_\ell \Rightarrow j_{\ell n} = \hbar(n_\ell + \mu_\ell) \quad (n_\ell = \text{integer}). \tag{29}$$

In equation (29) individual μ_ℓ can independently be taken in $[0, 1)$. Interestingly, Keller [33] uses single valuedness of the wave function (i.e. $\mu = 0$). For angle variables that assumption would lose the phase factors central to Keller's work. The difference is in the topology of the coordinate space: Keller's are simply connected, while $\{\theta\} \in [0, 2\pi]$, with identification of endpoints, is not.

For canonical variables such that $H = H(J_1, \ldots, J_N)$, the associated quantum operators commute. Using the quantized values of the J's and boldface for N-tuples, equation (29), gives the energy spectrum

$$E_{\boldsymbol{n}} = H(\hbar(\boldsymbol{n} + \boldsymbol{\mu})), \qquad n_\ell \text{ integers}, 0 \leqslant \mu_\ell < 1. \tag{30}$$

Nonzero μ is common: for the harmonic oscillator, $H = \omega_0 J$ and $\mu = 1/2$. The source of $\mu \neq 0$, which is to say, of non-single-valued $\psi(\theta)$, is the transformation from the original wave function (say) $\Psi(q)$ to the theta-valued wave function, $\psi(\theta)$.

The usual WKB fixes μ at $1/2$. From [33] one expects situations with $\mu = 1/4$. Nevertheless, as suggested by the path integral, there are other possibilities. When the underlying space is itself multiply connected the ordinary (not action-angle) wave function need *not* be single valued. Examples are the Aharonov–Bohm effect, Bloch functions in a periodic solid and SO(3) spin models [44, 45, 47]. In those cases a richer spectrum is available. However, for breathers in a solid, there is no reason to expect a homotopically nontrivial coordinate space.

4.3. KAM tori, the EBK method and stroboscopic reduction

The confinement seen in figure 7 is a restriction of the system to a small portion of the classical phase space. The restriction is even greater than is immediately evident: the orbit occupies only a two-dimensional hypersurface, a 2-torus. Regular motion on a torus lives on a hypersurface of up to half the dimension of the phase space [19][10]. As a result, functions of these variables and in particular the original canonical variables, are quasi-periodic functions with angular frequencies given by $\omega_k = \partial H/\partial J_k$, where the action-angle variables are $\{(J_1, \theta_1), (J_2, \theta_2), \ldots, (J_n, \theta_n)\}$. For almost all parameter values in the studies described below there was significant amplitude in only two frequencies, indicating a two-dimensional torus and confirming the visual implications of figure 11.[11] However, the toroidal structure manifest in the projection onto the space $\{Q_1, P_1, q_1, p_1\}$ hides a small sharing of excitation by other degrees of freedom, Q_2, etc. In particular, for 1% accuracy of the action it is vital to include contributions of atoms 3, etc. Labeling the action-angle variables for the torus (J_1, J_2), this implies that in principle these variables are functions of *many* of the original atomic coordinates, not just the first two.

Semiclassical quantization of *regular* motion has been studied using variants of EBK quantization [31–36, 38]. In our case, the absence of directly identifiable variables has

[10] Motion on a two-dimensional torus, means that only two of the Js are nonzero.

[11] Higher harmonics can also appear, due to nonlinearity, but in practice their amplitude is extremely low in our system. The torus topology does not depend on the absence of such harmonics.

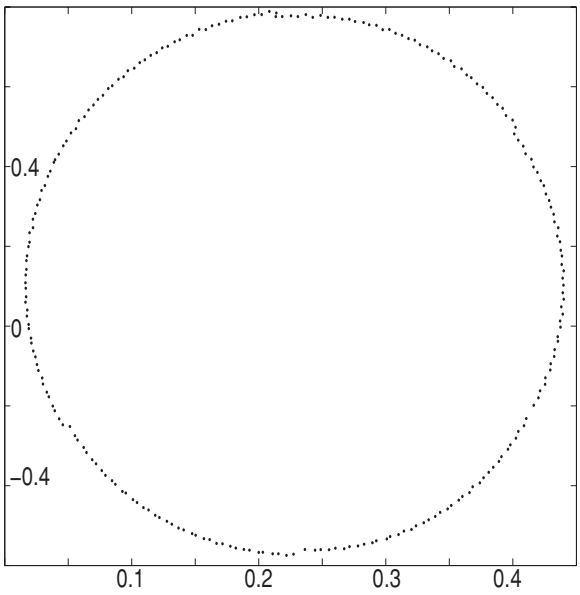

Figure 18. Projection on the Q_1–P_1 plane of the stroboscopically viewed KAM torus. There are 236 points taken for $299 \leqslant t \leqslant 679$ (in units of $1/\omega_0$).

prevented us from carrying over techniques in the literature. Nevertheless, we expect the semiclassical approximation to be effective: the frequencies of our breathers correspond to excitation energies of about 10–15 meV. Estimates based on the Stokes shift and on the width of the luminescence lines suggest that there is about 150 meV available to the breather, so that aggregate quantum numbers of about 10 are anticipated.

4.4. Calculating the action using a stroboscopic

The semiclassical breather program is now clear: numerically find the classical energy as a function of J. For each J an appropriate multiple of $\hbar$, one has a quantum energy level. Since the Js are unknown functions, one varies other parameters and evaluates the Js as a function of those parameters, varying *them* until the Js take the right values. At that point, one has the correct quantized energy levels (to $O(\hbar^2)$).

Finding the values of the Js for a given orbit requires evaluating $\sum \oint p\, dq/2\pi$ along curves that are topologically independent. This in turn requires a smooth curve of ps and qs. Such curves are obtained by looking at the orbit with a stroboscope. The pulse times for the strobe are found by Fourier transforming the orbit. Thus, if τ is a quasi-period of the orbit, one redoes the calculation and finds the phase space point at times of the form $t = m\tau$, with $m = 1, 2, \ldots$. (This is done for each quasi-period.) Recalling the action-angle characterization of the torus, this sets one of the angle variables equal to a constant and lowers the dimension of the torus by one. One thus obtains a loop for any phase space plane. For ps and qs corresponding to large excitation the loop is smooth and circle-like, but for smaller excitation can be quite rough. However, just because this is of lower excitation it does not seriously affect numerical accuracy. See figure 18 for a typical projection of this set on the Q_1–P_1 plane.

Table 1. Quantized energies.

$n_1 \downarrow, n_2 \rightarrow$	0	1	2	3
0	0.0269	0.0564	0.0864	0.1173
1	0.0522	0.0819	0.1121	0.1419
2	0.0772	0.1071	0.1370	0.1660
3	0.1028	0.1330	0.1629	0.1929
4	0.1278	0.1576	0.1880	0.2197
5	0.1531	0.1830	0.2135	0.2444
6	0.1786	0.2092	0.2392	0.2700
7	0.2043	0.2347	0.2651	0.2961
8	0.2296	0.2595	0.2903	0.3215
9	0.2550	0.2852	0.3173	0.3469
10	0.2800	0.3111	0.3414	0.3719
11	0.3069	0.3369	0.3679	0.3982
12	0.3315	0.3621	0.3928	0.4292
13	0.3572	0.3883	0.4252	0.4492

The EBK quantization condition, from equation (29), is $j_{n_\ell} = \frac{1}{2\pi}\sum_k \oint p_k \,\mathrm{d}q_k = \hbar\left(n_\ell + \frac{1}{2}\right)$, $\ell = 1, \ldots, N$, with $2N$ the dimension of phase space. Parameter counting shows that this condition selects more than just E: it completely determines the torus. This feature is central to our calculational strategy and can also provide a semiclassical approximation for the wave function. To find appropriate action values we studied a two-parameter family of initial conditions for the classical mechanics. These were selected so that only the breather was excited, which was accomplished as a corollary of confinement. (This ignores the zero-point energy of the other modes.) Using search methods described in detail [23], this allowed the quantization demand to be satisfied.

It is worth mentioning that our situation precludes use of the otherwise effective surface of section (SOS) method, which is often applied for EBK quantization. In that method things would be set up so '$\mathrm{d}q$' would be zero in the dimension orthogonal to that used in the calculation, and one could evaluate a single $\oint p\,\mathrm{d}q$ in the plane indicated. However, because our torus extends into several dimensions, fixing a single coordinate to be constant does not eliminate the need to evaluate other integrals. The full sum, $\sum \oint p\,\mathrm{d}q$, is over a particular phase space path and that path is picked in the plane of a well-formed oval, generally that of the Q_1–P_1 plane. Note that nearby points on the oval come at very different times, but this is irrelevant for the action calculation.

Figure 11 shows a projection onto the Q_1–P_1 plane of the points selected for the integration. One circle is used for each action calculation; about 2000 additional points are included to give perspective on the location of the rest of the torus.

4.5. Numerical results

Numerical values of energy versus action are given in table 1. A graph (as given in [23]) is less informative since the image is very nearly a plane. The parameters used were taken as approximations to those of KBr:Pb^{2+}, but as indicated earlier, cannot be considered part of a fundamental or *ab initio* theory. Parameters and units are given in the appendix.

A consistency check is available. The ωs are calculated from FFT, but by the principles of mechanics should also be given by $\partial H/\partial j$. We can evaluate the latter quantity using the

Table 2. Frequencies from FFT (averaged over $0 \leqslant n_1 \leqslant 13$) and from the slope of energy versus n_1 for fixed $n_2 = 0, 1, 2, 3$.

	$n_2 = 0$	$n_2 = 1$	$n_2 = 2$	$n_2 = 3$
FFT	3.2184	3.2273	3.2359	3.2444
Slope of $E/\hbar$	3.2188	3.2297	3.2624	3.2593

Table 3. Frequencies from FFT (averaged over $0 \leqslant n_2 \leqslant 3$) and from the slope of energy versus n_2 for fixed $n_1 = 0, 1, \ldots, 13$.

	$n_1 = 0$	$n_1 = 1$	$n_1 = 2$	$n_1 = 3$	$n_1 = 4$	$n_1 = 5$	$n_1 = 6$
FFT	3.7977	3.8070	3.8159	3.8254	3.8345	3.8432	3.8520
Slope of $E/\hbar$	3.8111	3.7930	3.7528	3.8003	3.8748	3.8564	3.8527
	$n_1 = 7$	$n_1 = 8$	$n_1 = 9$	$n_1 = 10$	$n_1 = 11$	$n_1 = 12$	$n_1 = 13$
FFT	3.8606	3.8691	3.8774	3.8855	3.8938	3.9022	3.9105
Slope of $E/\hbar$	3.8722	3.8805	3.8979	3.8739	3.8617	4.0994	3.9604

independently calculated energies and action values. This therefore serves as a check on those calculations. In table 2 we show the slopes of the energy (divided by $\hbar$)[12] as a function of n_1 and compare these to the average ω_2 values for the corresponding initial condition set. The same is done for energy slopes for fixed n_1 and $0 \leqslant n_2 \leqslant 3$. Although there are fewer points, the consistency is good and the results presented in table 3. Other self-consistency checks can be found in [23].

For all data presented above, the value of q_0, the 'push' on the chain due to the JT distortion of the Pb, was taken to be unity (1 Å). This was based on rough estimates of displacements, but may be a bit high. When ω_0 is derived from ω_{Debye} (as described in the appendix), a value of q_0 that better matches the available energy is 0.75; however, in a run in which all atoms begin at 0, this yields little excitation in the second breather mode, with less opportunity to study that aspect of the problem. Moreover, if ω_0 is instead derived from the bulk speed of sound, one finds that $q_0 = 1$ is the better choice. In any case, for our systematic study we chose the latter value. In general though, as one moves toward better modeling of the actual experiments, an improved potential should be sought, based on matching speed of sound, band gaps [48] and other properties.

5. Stability of quantum breathers

The lifetime of the quantum breather against decay is an issue of experimental relevance. At the classical level, both analytical and numerical experience support an infinite lifetime, at least for the one-frequency breather [49]. In a diatomic lattice there are two breather frequencies and, in principle, combinations of these modes can allow energy to leave via the phonons. In our simulations, as shown in section 3.3, this does not take place in any perceptible way.

But classical stability does not guarantee its quantum counterpart. Quantum tunneling bypasses classical constraints, and, for a translationally invariant system, insures that bound states that are not of finite support become bands. Indeed such bands—as well as tunneling—have been studied for breathers in a homogeneous lattice [50–52]. Other breather quantization approaches have also been taken, including semiclassical, as described in section 4, and field-theoretical [53]. In the semiclassical approach one studies the torus-confined classical

[12] The calculation is entirely classical; the $\hbar$ enters only because the action (j) values we use are spaced by $\hbar$.

trajectory. This yields a stable state, since, just as for a 1D state hidden behind a barrier, the classical trajectory does not sense the possibility of escape. Our expectation is that the decay rate should be of the form exp(−[positive constant]/$\hbar$), just as for one-dimensional tunneling. This reflects the absence of a stationary point in the functional integration, and, as in finite-dimensional asymptotics when a stationary point is absent and the endpoints of integration are infinite, one can only get contributions that vanish faster than any power of the asymptotic (going to zero) parameter.

The stability of quantum breathers has been controversial, with some authors [54] claiming that breathers in alkali halides should have lifetimes on the order of 10 ns. (They also appear to claim $O(\hbar^2)$ decay, contradicting the semiclassical expectations mentioned above.) Subsequent work [55] challenged this estimate and suggests stability in the limit of large systems. Our calculations [56, 57], using two methods, confirm stability. For the purpose of this 'stability debate' we only considered monatomic chains, since the claims of quantum decay had been made for this (simpler) system.

The system is a ring of $N + 1$ unit-mass atoms with Hamiltonian

$$H = \sum_{k=0}^{N} \left\{ \frac{1}{2} p_k^2 + \frac{1}{2}\omega_s^2 x_k^2 + \frac{1}{2}\omega_0^2 (x_k - x_{k+1})^2 + \frac{1}{4}\lambda x_k^4 \right\}, \qquad x \in \mathbb{R}. \tag{31}$$

Periodicity is expressed through $x_0 \equiv x_{N+1}$ and mod-(N+1) addition for atom labels. This is the nonlinearity studied in [50]. Another system, closer to our own models, is

$$\widetilde{H} = \sum_{k=0}^{N} \left\{ \frac{1}{2} p_k^2 + \frac{1}{2}\omega_s^2 x_k^2 + \frac{1}{2}\omega_0^2 (x_k - x_{k+1})^2 + \frac{1}{4}\lambda (x_k - x_{k+1})^4 \right\}, \tag{32}$$

also periodic. This system was studied in [57], but will not be discussed in this review, since the results closely parallel those of equation (31).

We next make a significant calculational simplification, but one that does not affect the in-principle issue of quantum stability, or at least insofar as that principle was called into question by [54], since it is effectively the same approximation that is used there. Specifically, we drop all nonlinearity except that affecting particle 0. This is based on the observation that all atoms other than 0 (for the monatomic chain with the parameters we use) hardly move, and in particular are well within the regime where nonlinear effects are negligible. With this assumption the Hamiltonian corresponding to equation (31) is

$$H = \sum_{k=0}^{N} \left\{ \frac{1}{2} p_k^2 + \frac{1}{2}\omega_s^2 x_k^2 + \frac{1}{2}\omega_0^2 (x_k - x_{k+1})^2 \right\} + \frac{1}{4}\lambda x_0^4. \tag{33}$$

One can compare the classical orbits that result from the Hamiltonian of equation (32), with full nonlinearity, and those resulting from equation (33). Plots of position and kinetic energy are nearly indistinguishable. To see any difference one should look at the Fourier transform of position, figure 19. For the fully nonlinear equations, there is excitation of higher harmonics, but it is down in magnitude by several orders of magnitude from the principal oscillation.

Remark. Note that this Hamiltonian automatically eliminates the issue of decay via bands, which for our breather is irrelevant (our system is not translationally invariant) and in general is small.

To deal with equation (33), we used two distinct approaches, having at their core fundamentally different approximations. The first is numerical diagonalization, similar to Wang *et al* [50], and in which we incorporated methods to reduce cutoff effects and to provide

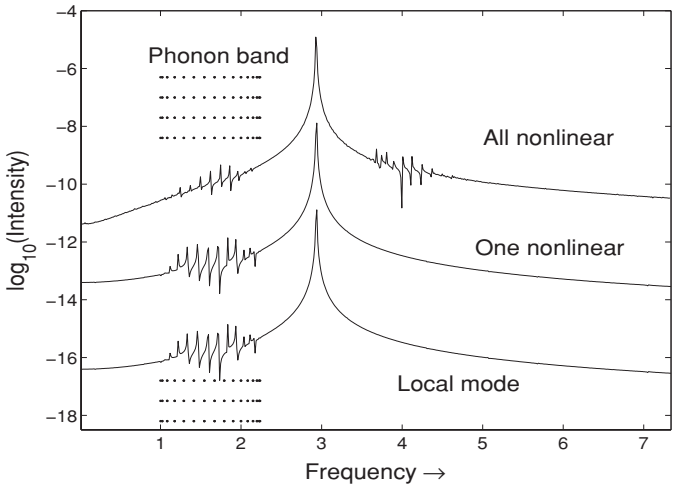

Figure 19. Fourier transform of the first atom; comparison of the full nonlinear model with the only 0 nonlinear and linear mode approximations. The 'one nonlinear' plot is displaced downward by 3 and the 'local mode' plot by 6. Dotted lines indicate the span of the phonon band.

direct evidence of localization. The second is a path integral calculation, treating the breather fully quantum mechanically, similar to Feynman's polaron [58]. The approximation for the calculations in this case is semiclassical asymptotics.

For both these approaches, albeit for slightly different objectives, we find it useful to introduce a *local mode*. That is, we consider the Hamiltonian

$$H_0 = \sum_{k=0}^{N} \left\{ \frac{1}{2} p_k^2 + \frac{1}{2}\omega_s^2 x_k^2 + \frac{1}{2}\omega_0^2 (\Delta x)_k^2 \right\} + \frac{1}{2}\omega_1^2 x_0^2 \tag{34}$$

which, with a good choice of ω_1, will bear a strong, but not perfect resemblance to the breather. This local mode is linear and thus has true, non-decaying, eigenstates localized at the site 0.

5.1. Numerical diagonalization

For numerical diagonalization the Hamiltonian (33) is made finite-dimensional by using a phonon basis and imposing a cutoff on the level of phonon excitation. A low cutoff is needed because of the proliferation of dimensions in the (implicit) tensor product of phonon operators. The same problem was faced in [50].

We found that introducing a local mode and perturbing around that made for a significant reduction in the number higher order phonons needed in the perturbation expansion. The Hamiltonian is thus split in the following way:

$$H = \sum_{k=0}^{N} \left\{ \frac{1}{2} p_k^2 + \frac{1}{2}\omega_s^2 x_k^2 + \frac{1}{2}\omega_0^2 (\Delta x)_k^2 \right\} + \frac{1}{4}\lambda x_0^4 = H_0 + V_I, \tag{35}$$

with H_0 given in equation (34) and

$$V_I \equiv \tfrac{1}{4}\lambda x_0^4 - \tfrac{1}{2}\omega_1^2 x_0^2. \tag{36}$$

In figure 20 we give a one-dimensional example exhibiting the benefits of this split.

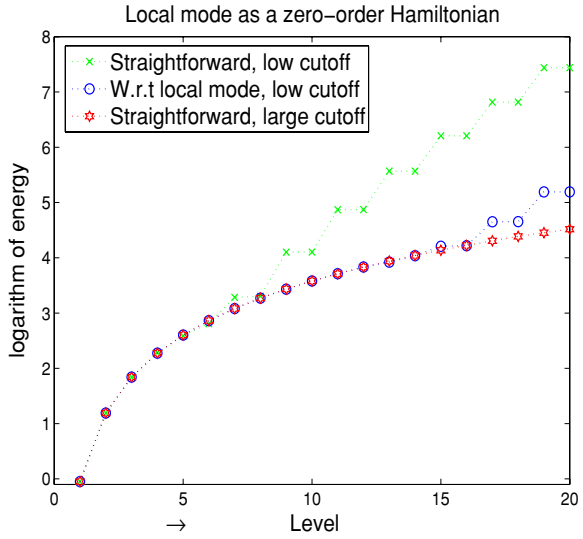

Figure 20. Advantage of using a local mode for perturbation theory. Let $H_0 = p^2/2 + x^2/2$, $V_4 = \lambda x^4/4$, $V_2 = \omega_1^2 x^2/2$, $V_{4\,\mathrm{minus}\,2} = V_4 - V_2$. For this graph we use $\lambda = 8$ and $\omega_1 = 3$. The curve marked 'straightforward, low cutoff' results from perturbing H_0 by V_4, with operators in the number representation cut off at 20. The curve marked 'w.r.t. local...' takes $H_0 + V_2$ as the 'zero-order' Hamiltonian and perturbs it by $V_{4\,\mathrm{minus}\,2}$ with the same cutoff, 20. This parallels our method for the larger ring problem. Finally the curve marked 'large cutoff' results from perturbing H_0 by V_4 but with a much larger cutoff (1 0 0), yielding results that are reliable (to the accuracy of the graph) for levels 1 through 20. Note that the figure shows the logarithm of the energy eigenvalues.

We will not go into the details of the calculation, as it consisted of fairly standard expansions about our favorable basis states. Beyond the local mode simplification we also noted a reflection symmetry about atom 0, which allowed a nearly factor 2 reduction in the dimension. The parameters we used were $\lambda = 8$, $\omega_0 = 1$ and $\omega_s = 1$ (used in [50]), and for $\omega_1 = 2.5$ the true eigenfunction having greatest overlap with the first excited state of the local mode is shown in table 4. Clearly the local mode dominates. The next largest component is the thrice excited local mode, which is merely a shape adjustment. Other modes barely make the 10^{-3} level. Note that the highest excitation level for *other* phonons is 3, indicating that a cutoff of 6 is safe. In fact, even to probability 10^{-8} there is no excitation higher than 3 except for the local mode.

Remark. For nearest-neighbor nonlinearity the story is the same. A systematic study of a size-8 ring with cutoffs of 6, 8 and 12, showed that the local mode dominated the Hamiltonian's ground state.

Remark. In [57] details of this calculation are given. Many more states are exhibited and a comprehensive study of cutoff dependence provided.

Our conclusion is that the breather is almost entirely dominated by the local mode, and like it, stable. In [57] we also looked explicitly at time dependence. The most serious limitation in our demonstration is the size of the system. Although we have not diagonalized our system for rings of 14 spins, it is nevertheless possible to calculate the principal matrix element that expresses the nonlinearity. The initial state of interest is that having a single excitation of

Table 4. Principal components of the breather state. The first four columns refer to the four symmetric phonons in a 6-atom ring. Row 1: frequencies (local mode is highest). Subsequent rows: number-operator values. Fifth column: norm squared of the mode ($\log_{10}$ in parentheses). Cutoffs: local mode 13, others 6. For this state first-order perturbation theory is good to 0.3%. The last column reports the same calculation with cutoff 8.

0.749	0.987	1.19	2.04	Prob. (6)	Prob. (8)
0	0	0	1	0.9947	0.9952
0	0	0	3	3.315 (−3)	3.321 (−3)
0	1	0	0	1.122 (−3)	0.848 (−3)
0	0	1	0	5.748 (−4)	4.345 (−4)
1	0	0	0	1.545 (−4)	1.167 (−4)
0	1	0	2	1.004 (−4)	0.754 (−4)
1	0	0	2	2.866 (−5)	2.152 (−5)
0	0	1	2	2.303 (−5)	1.728 (−5)
0	0	0	5	3.670 (−6)	3.627 (−6)

the local mode: $|\text{local}\rangle \equiv |0, 0, 0, \ldots, 1\rangle$ where the '1' refers to the eigenvalue of the local mode number operator and the zeros to other phonon levels. This state couples to those in the continuum via the matrix element

$$g(n_1, n_2, \ldots) \equiv \langle \text{local}|x_0^4|n_1, n_2, \ldots\rangle. \tag{37}$$

In figure 21 is a logarithmic plot of g as a function of energy. The pattern seen in this figure is that for a ring of 14 oscillators. It is the same as one sees for 4, 6, 8 or any number that we have been able to study. As such the substantial overlap of the true eigenstate—induced by the nonlinear λ—with the local mode—induced by ω_1—should continue as system size grows, since it is these matrix elements that determine the overlap.

5.2. Path integral approach

Our use of the path integral in this problem exploits an application of that technique that goes back to Feynman's treatment of the polaron [58, 59], one of the early triumphs of functional integration. It is based on one of the most useful features of the path integral: the propagator for a quadratic degree of freedom coupled linearly to something else can be evaluated explicitly, leaving only a self-coupling of that other degree of freedom. The penalty is the nonlocality in time of the self coupling, the reward the reduction of the problem to a single degree of freedom.

As for the numerical integration approach (section 5.1), it will prove useful to introduce a (quadratic) *local mode*. In this case its function will be used as a benchmark for localization. We know that with a local mode the reduced dynamical system (reduced à la Feynman, as just discussed) has a localized ground state; we will find the same to be true for the nonlinear system.

5.3. Setting up the path integral

The Lagrangian associated with the Hamiltonian (33) is

$$\mathcal{L} = \frac{1}{2}\sum_{n=1}^{N+1}\dot{x}_n^2 - \frac{1}{2}\omega_0^2\sum_{n=1}^{N+1}(x_n - x_{n+1})^2 - \frac{1}{2}\omega_s^2\sum_{n=1}^{N+1}x_n^2 - \frac{\lambda}{4}x_0^4 + \mu x_0(x_m + x_{N+1-m}). \tag{38}$$

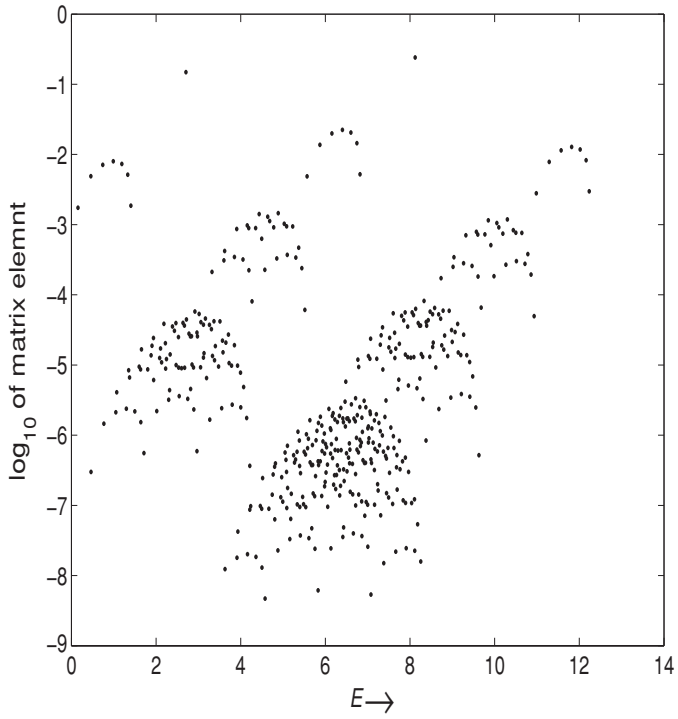

Figure 21. Base-10 logarithm of $|\langle 0, 0, \ldots, 0, 1|x_0^4|n_1, n_2, \ldots\rangle|$ for a ring of 14 oscillators. States, $|n_1, n_2, \ldots\rangle$, are ordered by increasing energy.

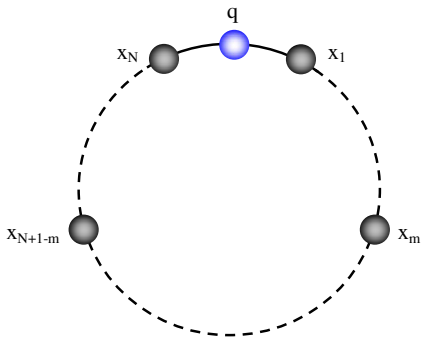

Figure 22. Selected atoms on the ring. For convenience the notation q is used for x_0.

We have introduced an additional term, $\mu x_0(x_m + x_{N+1-m})$, which allow us to study correlations. The derivative (at $\mu = 0$) of the (appropriate form of the) propagator provides a 0-m-correlation. We will take particle m to be distant from 0, typically about $1/3$ of the way around the ring. The use of a pair (m and $(N + 1 - m)$) maintains mirror symmetry with respect to particle 0. We will also distinguish between the *ring*, all $N + 1$ atoms, and the *chain*, atoms 1 through N (see figure 22).

The Lagrangian $\mathcal{L}$ can be written in the form $\mathcal{L} = \mathcal{L}_0 + \mathcal{L}_C + \mathcal{L}_I$. Here $\mathcal{L}_0$ is the Lagrangian of particle 0

$$\mathcal{L}_0 = \frac{1}{2}\dot{q}^2 - \left(\omega_0^2 + \frac{1}{2}\omega_s^2\right) q^2 - \frac{\lambda}{4} q^4, \tag{39}$$

where we have adopted the notation q for x_0. $\mathcal{L}_C$ is the Lagrangian of the chain

$$\mathcal{L}_C = \frac{1}{2}\sum_{n=1}^{N} \dot{x}_n^2 - \frac{1}{2}\omega_0^2 \sum_{m,n=1}^{N} J_{mn} x_m x_n - \frac{1}{2}\omega_s^2 \sum_{n=1}^{N} x_n^2, \tag{40}$$

with $J_{mn} = 2\delta_{mn} - \delta_{m+1,n} - \delta_{m,n+1}$ $(m, n = 1 \ldots N)$, the Jacobi matrix. The last term $\mathcal{L}_I$ is the interaction between particle 0 and the others

$$\mathcal{L}_I = \omega_0^2 q\,(x_1 + x_N) + \mu q (x_m + x_{N+1-m}). \tag{41}$$

We perform the path integral for the chain and arrive at an effective action and path integral for q alone [45, 58, 60, 61]. The result of these standard calculations is

$$\mathcal{G}(q^f, T; q^i, 0) = \int \mathcal{D}q e^{\frac{i}{\hbar}(S_0 + S_{\text{eff}})}, \tag{42}$$

where the action S_0 arises from the original $\mathcal{L}$ sans chain terms, specifically

$$S_0 = \int \mathrm{d}t \left\{ \frac{1}{2}\dot{q}^2 - \left(\omega_0^2 + \frac{1}{2}\omega_s^2\right) q^2 - \frac{\lambda}{4} q^4 \right\}. \tag{43}$$

The effective action, S_{eff}, is the result of the integration just described over chain degrees of freedom. It is given by

$$S_{\text{eff}} = \int_0^T \int_0^T \mathrm{d}t\, \mathrm{d}s\; K(|t - s|) q(t) q(s), \tag{44}$$

with

$$K(u) = \sum_{n=1,3,\ldots}^{N} \tau_n^2 \frac{\cos \Omega_n \left(\frac{T}{2} - u\right)}{\Omega_n \sin\left(\frac{\Omega_n T}{2}\right)}, \tag{45}$$

and

$$\tau_n \equiv \sqrt{\frac{2}{N+1}} \left(\omega_0^2 \sin \frac{\pi n}{N+1} + \mu \sin \frac{\pi n m}{N+1} \right). \tag{46}$$

We shall study the (matrix element of the) propagator in the stationary phase approximation; that is, we focus on the action (including S_{eff}) along the extremal 'classical paths'.

Let us return for a moment to the formulation in terms of all degrees of freedom in order to appreciate what information is contained in $\mathcal{G}$. The spectral expansion of the full propagator—a function of *all* variables—is

$$G(x_0'', x_1'', \ldots, t; x_0', x_1', \ldots) = \sum_{\alpha} \Phi_\alpha(x_0'', x_1'', \ldots) \exp(-i E_\alpha t) \Phi_\alpha^*(x_0', x_1', \ldots), \tag{47}$$

where α is an eigenstate label. This implies that the subsequent operations in deriving equation (43) lead to

$$\mathcal{G}(q'', t; q', 0) = \exp\left(+\mathrm{i} \sum \Omega_n t/2\right) \sum_{\alpha} \phi_\alpha(q'') \exp(-\mathrm{i} E_\alpha t) \phi_\alpha^*(q'), \tag{48}$$

where

$$\phi_\alpha(q) \equiv \int \Psi_0(x_1, \ldots)^* \Phi_\alpha(q, x_1, \ldots)\, \mathrm{d}x_1 \ldots, \tag{49}$$

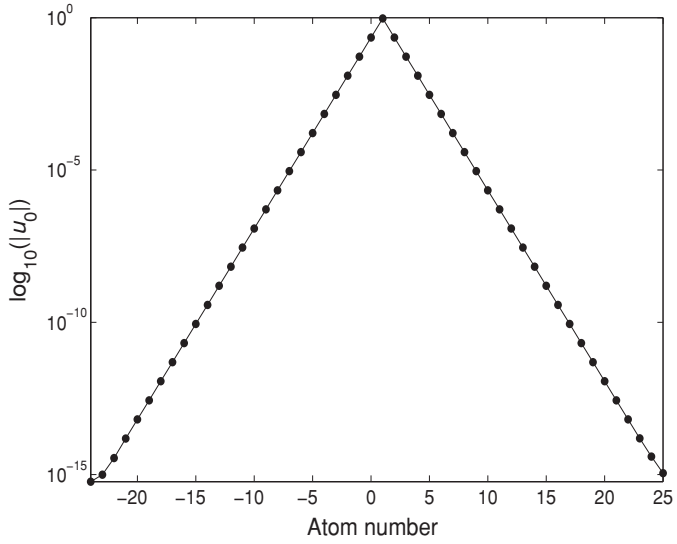

Figure 23. The classical local modes are $u_\ell(n)$, with ℓ the mode label and n the atom. Shown in the figure is the base-10 logarithm of the absolute value of mode 0, the local mode. Parameters are $\omega_1 = 2$ and $\omega_0 = 1$ (cf equation (34)). Clearly there is an exponential dropoff of excitation for the atoms.

and Ψ_0 is the ground state of the chain. Note that E_α in equation (48) is the total energy of the ring, while $E_C \equiv \sum \Omega_n/2$ is the total ground state energy of the chain. Going to imaginary time, $t = -\mathrm{i}T$ equation (48) becomes

$$\widetilde{\mathcal{G}}(q'', T; q', 0) = \sum_\alpha \phi_\alpha(q'') \exp[-(E_\alpha - E_C)T]\phi_\alpha(q')^*. \tag{50}$$

Our use of equation (50) will be to study eigenstates. Although the Hamiltonian obviously has eigenstates, we do not know whether they resemble breathers, that is to say, whether there is localization. Our goal then is to show that for some true eigenstates the amplitude is concentrated near particle 0.

To see how to do this, we will consider first a *local mode*, a quantum state that we know to be localized. Thus we will repeat the path integral calculation for the Hamiltonian equation (35), and in equation (38) will replace the 4th power by a quadratic. Specifically, the classical mode function has a sharp spatial dropoff and the quantum state represents atomic oscillations with that pattern. For reference we show the classical local mode for $\omega_1 = 2$ and $\omega_0 = 1$ in figure 23 (a solution of equation (34)). (The value of ω_s does not affect the function.)

Our goal then is to ascertain properties of ϕ_α and E_α from the semiclassical approximation to G. However, for both the linear and nonlinear cases, implementing the semiclassical approximation presents technical challenges, which we now discuss.

5.4. Methodology

The first observation to be made is that the development from equation (38) to equation (50) goes through in exactly the same manner, with the same K, etc, for the quadratic local mode as for the nonlinear excitation, with the sole exception of the final form of S_0, which, for the local

mode case, has a term $\omega_1^2 q^2/2$ instead of $\lambda q^4/4$. Going over to imaginary time, our problem revolves about the following quantities:

$$S_{\text{total}} = \int_0^T \mathrm{d}t \left\{ \frac{1}{2}\dot{q}^2 + \frac{1}{2}\left(\omega_s^2 + 2\omega_0^2\right)q^2 + U(q) \right\} - \int_0^T \int_0^T \mathrm{d}t\, \mathrm{d}s\, \widetilde{K}(|t-s|)q(t)q(s), \tag{51}$$

where $U(q) = \omega_1^2 q^2/2$ for the local mode problem. The same form holds for the nonlinear problem as well, but with $U(q) = \lambda q^4/4$. S_{total} is the total classical action, and in the path integral appears as $\exp(-S_{\text{total}})$ (note the minus sign, a result of the $t \to -it$ transformation). The self-interaction kernel becomes

$$\widetilde{K}(u) = \sum_{n=1,3,\ldots}^{N} \tau_n^2 \frac{\cosh \Omega_n \left(\frac{T}{2} - u\right)}{\Omega_n \sinh\left(\frac{\Omega_n T}{2}\right)}, \tag{52}$$

with the same τ_n as in equation (46). The classical equation of motion follows from the usual variational methods and is

$$\ddot{q} - \left(\omega_s^2 + 2\omega_0^2\right)q - \frac{\partial U}{\partial q} + 2\int_0^T \widetilde{K}(|t-s|)q(s) = 0. \tag{53}$$

For the semiclassical approximation one must solve equation (53). We used different methods for the linear and nonlinear cases, and discuss them separately.

5.4.1. Linear, non-local in time propagators. For $U(q) = \omega_1^2 q^2/2$, equation (53) can be discretized, say with $t_k = k\epsilon$, $k = 0, 1, \ldots, M+1$, $\epsilon = T/M$. q becomes a vector, $q_k = q(t_k)$ $(k = 1, \ldots, M)$ and the entire equation has the form $Bq = q_0$,[13] with B a matrix consisting of three parts: the second derivative operator, $2/\epsilon^2$ on the diagonal, $-1/\epsilon^2$ above and below; a diagonal matrix proportional to $\left(\omega_s^2 + 2\omega_0^2\right)$ and a matrix (which by a slight abuse of notation we call) K whose substantial non-diagonal components reflect the nonlocality in time. From equation (53) it may not be evident how a nonzero right-hand side (q_0) comes into the picture. It arises from the boundary conditions. When discretizing, the first and last rows of the second derivative operator call on q-components outside the range $1, \ldots, M$. These other components are the boundary values (call them $a = q_{\text{initial}}$ and $b = q_{\text{final}}$), so that $q_0(1) = -a/\epsilon^2$ and $q_0(M) = -b/\epsilon^2$ (other components of q_0 are zero). This method of dealing with the two-time boundary value problem is a simpler version of what is done in [62]. It follows that the solution of the nonlocal-in-time equations of motion is $q = B^{-1}q_0$. It is also immediate that for this linear equation the action along this 'classical path' is given by $S = [q(t)\dot{q}(t)/2]|_0^T$, although one can also evaluate S by explicit integration.

The nonlocality in time means that the matrix K is not sparse, putting a limit on the smallness of ϵ, hence on the accuracy of the action. This was overcome by extrapolating in ϵ. Call $S(\epsilon)$ the action that results from the discretization and matrix inversion with a given ϵ. Expand in ϵ: $S(\epsilon) = S(0) + \epsilon S'(0) + \epsilon^2 S''(0)/2 + \cdots$. By evaluating $S(\epsilon)$ for several values of ϵ one can then extrapolate to zero. We typically used three values.

As described in detail in [57], the accuracy of this method was tested against known analytic results both for the harmonic oscillator and in the asymptotics of $\phi_0(q)$ (as defined in equation (49)). Excellent agreement was found.

5.4.2. Nonlinear, non-local in time propagators. With a nonlinear term in the action, the classical nonlocal two-time boundary value problem cannot be solved by matrix inversion.

[13] This q_0 is not the same as that used in our dynamical simulations.

The equation to be solved is

$$\ddot{q} - \left(\omega_s^2 + 2\omega_0^2\right)q - \lambda q^3 + 2\int_0^T \widetilde{K}(|t-s|)q(s) = 0. \tag{54}$$

Our method is an extension of Feynman's approach [58] in which the introduction of an auxiliary variable eliminates the nonlocality. Then one can use standard numerical methods for solving the two-time (even-if-nonlinear) boundary value problem. Recalling the definition of $\widetilde{K}$, equation (52), one can define auxiliary variables z_n by

$$z_n(t) \equiv \int_0^T \mathrm{d}s \frac{\cosh\Omega_n\left(\frac{T}{2} - |t-s|\right)}{\Omega_n \sinh\left(\frac{\Omega_n T}{2}\right)} q(s). \tag{55}$$

equation (54) becomes

$$\ddot{q} - \left(\omega_s^2 + 2\omega_0^2\right)q - \lambda q^3 + 2\sum_n \tau_n^2 z_n = 0. \tag{56}$$

Taking two derivatives of z_n leads to

$$\frac{\mathrm{d}^2 z_n}{\mathrm{d}t^2} = \Omega_n^2 z_n - 2q(t), \qquad n = 1, 3, \ldots, 2\left[\frac{N-1}{2}\right] + 1. \tag{57}$$

One non-local equation has been replaced by a larger number of local ones. There is but a single pair of boundary conditions: $q(0) = a, q(T) = b$. The conditions on z are forced by self-consistency arising from equation (55), which incidentally also imply $z_n(0) = z_n(T)$, for all n. It is amusing that with the quartic interaction replaced by a quadratic one, this linear system is equivalent to the set of classical linear equations that apply to the ring, with the boundary conditions inherited from the ground state averaging (which is of course where equation (54) (made linear) comes from in the first place).

For numerical solution of equation (54), we noted that for large N and T, one could get 10^{-4} accuracy with the approximation $\widetilde{K}_1(u) \equiv \widetilde{K}(0)\cosh(\omega_{\mathrm{eff}}u)$, for a judicious choice of ω_{eff}.

With this approximation for $\widetilde{K}_1$, only a single z need be defined, so that our nonlocal equation becomes a pair of second-order ODE's, with boundary values for one of them and a self-consistency condition for the boundaries of the other. Using the optimal ω_{eff}, the equations are

$$\ddot{q} = \left(\omega_s^2 + 2\omega_0^2\right)q + \lambda q^3 - 2z, \tag{58}$$

$$\ddot{z} = \omega_{\mathrm{eff}}^2 z - 2q(t), \qquad \text{with} \qquad z(t) \equiv \int_0^T \mathrm{d}s \frac{\cosh\omega_{\mathrm{eff}}\left(\frac{T}{2} - |t-s|\right)}{\omega_{\mathrm{eff}} \sinh\left(\frac{\omega_{\mathrm{eff}} T}{2}\right)} q(s). \tag{59}$$

The boundary values of $q(t)$ are given. For z one proceeds iteratively. For given $z(0)$ $(=z(T)$, by definition), the boundary value problem can be solved by standard methods. Using that solution, $q(t)$, one recomputes $z(0)$. In effect one has a function mapping $z(0)$ into a new value, and a fixed point of the map can be found numerically. That fixed point solves the original boundary value problem for q.

To improve on this solution, we noted that the true solution of the classical nonlinear, nonlocal problem minimizes the action, S. This suggesting modifying the $q(t)$ derived above so as to further reduce S. The class of perturbations for this purpose can be narrowed by the following consideration. The potential that we study is an inverted oscillator, linear or nonlinear. Therefore, if the time interval for going between two not-too-small boundary values is large, for most of that time interval the particle will be near zero, with zero velocity:

the path is thus an *instanton* and, except near the endpoints, will be exponentially small (in T). S-reducing variations of q will thus have the same shape. Our basic variation consists of adding and subtracting hyperbolic cosine functions with varying amplitudes and angular frequencies.

When this procedure was implemented, the resulting changes in S were extremely small. The first correction was on the order of 10^{-5} of the action, and subsequent reductions were of order 10^{-15}. No other functional forms (e.g. multiplying instanton-shaped curves by oscillatory functions) gave any improvement at all. The results presented below use this method of optimizing S.

It is also possible to perform some of the checks made on the linear problem. In particular the asymptotic form of the wave function for a quartic anharmonic oscillator is $\psi \sim \exp(-[\text{positive const} \cdot q^3])$. With various λ we found the action for large boundary values of q; there was a very good fit to the cubic.

5.5. Localization

The local mode represents a localized excitation. Figure 23 shows the classical mode oscillation amplitude, hence the shape of the phonon; in particular it indicates an exponential dropoff with distance from the center of the mode. We will use our path integral formalism to show how it too reflects the localization of the 'local mode'. Then we will use the same technique to establish the localization of the *nonlinear* breather wave function.

The key is the coupling, $\mu x_0(x_m + x_{N+1-m})$, inserted in the Lagrangian of equation (38). Site m is taken far from site 0, where the large oscillations of the breather are taking place. A derivative with respect to μ at $\mu = 0$ provides the correlations we seek in the following way. The imaginary-time version of equation (42) is

$$\mathcal{G}(q^f, T; q^i, 0) = \int \mathcal{D}q \, \mathrm{e}^{-S_{\text{total}}/\hbar}, \tag{60}$$

where S_{total} is given by equation (51), and $\widetilde{K}$ by equation (52) (equation (51) is valid for both quadratic and quartic potentials). Note that the μ-coupling appears in the definition of τ_n (equation (46)), and *only* there.

Thinking back to the propagator before the integration over chain mode ground states, we consider the derivative $\partial G(a, -\mathrm{i}T; a)/\partial\mu|_{\mu=0}$. The importance of this derivative arises from the relation

$$\langle A \rangle = \frac{\partial}{\partial \mu}\left[\int \exp(-S + \mu A)\,\mathrm{d}x\right]\Bigg|_{\mu=0} \Bigg/ \int \exp(-S)\,\mathrm{d}x, \tag{61}$$

where $\exp(-S)$ is a weight for averaging. Since we are taking $\partial/\partial\mu$ after integrating, we are getting an average of the $\langle q x_m \rangle$-correlation in the chain mode ground state[14].

In the semiclassical approximation (which is exact in the linear case), the study of $\partial G(a, -\mathrm{i}T; a)/\partial\mu|_{\mu=0}$ is essentially the same as the study of $\sigma(a, T, g) \equiv \partial S(a, T)/\partial\mu|_{\mu=0}$, where '$S$' is the imaginary time action, a is the common initial and final endpoint, and T the imaginary time. The quantity g, implicit in $S(a, T)$, parameterizes the relevant particle 0 enhancement; for the linear local mode it is ω_1 and for the quartic case it is λ.

Consider first $\sigma(a, T, \omega_1) \equiv \partial S(a, T)/\partial\mu|_{\mu=0}$ for moderate T (such that states other than the ground state survive in the spectral sum for $\mathcal{G}$), for small ω_1 and for large a. Because a is large, the important terms in the spectral sum will not be those of lowest energy, but those that

[14] Of course what we call the $\langle q x_m \rangle$-correlation is really the $\langle q(x_m + x_{N+1-m})\rangle$-correlation (or $\langle q(x_m + x_{-m})\rangle$). Note too that there is no mathematical problem in exchanging the order of operations in equation (61).

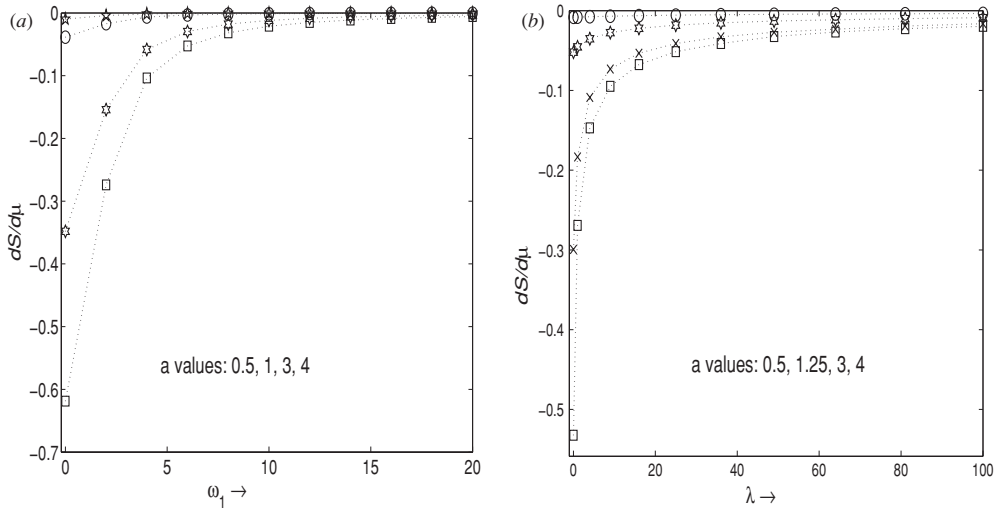

Figure 24. $\mathrm{d}S/\mathrm{d}\mu$ (essentially a correlation function) has markedly different behavior for large and small endpoint values (a or a in the figure) for q. Shown on the left, figure 24(a), is the effect of varying a and ω_1 for the linear local mode, while on the right, figure 24(b), are the corresponding graphs for variation of a and λ in the nonlinear mode. Both for a linear local mode (as a function of ω_1) and for the breather (function of λ), a large value of a demands relatively large correlations when neither a local mode nor a breather is present ($\omega_1 \sim \lambda \sim 0$), but that correlation is wiped out for large parameter (λ or ω_1), for which the breather or local mode is effectively decoupled from the rest of the ring.

permit large excursions of q (cf equations (48) and (49)). However, since ω_1 is assumed small, there will be no local mode. So pulling q far from its equilibrium position, pulls *all* atoms far from their positions, and the correlation of atom 0 (q) and atom m (x_m) should be large. On the other hand, suppose ω_1 to be large (with a still large and T moderate). In that case there is a pronounced local mode and pulling q away from equilibrium has little impact on x_m. For the local mode, q can have large excursions while other atoms hardly move. Therefore, one expects σ to be small. In figure 24(a), the lowest curve shows just this behavior. The boundary value of q, a, is 4 and for small ω_1 (no local mode) there is a large correlation with the motion of atom-m (0 is at the *top* of the figure). As ω_1 increases, this correlation shrinks.

By contrast, if a is small, the variation of ω_1 has little effect. This can be understood as follows. The requirement on the endpoints of q imposes little demand on any other coordinates whether or not there is a local mode.

We next turn to the nonlinear case. Here we do not have *a priori* knowledge of the wave function but can use the correlation function as a test of localization. The behavior of the correlation function, as a function of a and λ exactly parallels that of the linear local mode. This is shown in figure 24(b). For small λ and large a there is no breather and, as for the small ω_1 case, the demand for a large excursion of q forces a large excursion of x_m. And now the central observation: for large λ, forcing q to be large has almost no impact on x_m, exactly as for the quadratic local mode, from which we deduce the localization of the breather excitation. We remark that corresponding values of ω_1 and λ are related by $\lambda \sim \omega_1^2$.

We mention that one can make similar deductions about correlations from the T-dependence of $\mathrm{d}S/\mathrm{d}\mu$. For details, see [57].

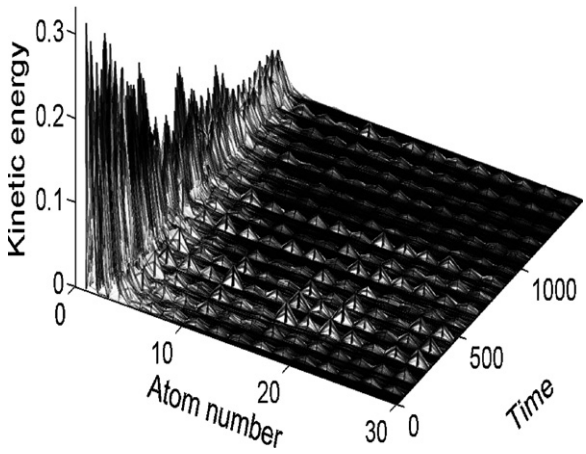

Figure 25. Kinetic energy of the system interacting with a transverse phonon as a function of time and atom number.

This establishes that the true eigenfunctions for which q has large displacements are localized (when the coupling is strong). Since these are the true eigenfunctions, the quantum breather is stable.

6. Breathers and noise/temperature

6.1. Temperature dependence of the decay anomaly

Experimentally [15], the decay anomaly is most pronounced at low temperature. With increasing temperature it weakens and is extinguished around 100–150 K, depending on the crystal. As shown in section 2.1.2, here too the slow relaxation assumption explains the anomaly. In view of the breather-induced inhibition of relaxation at low temperature, it is natural to expect that the temperature dependence of the anomaly should be a consequence of thermal effects on the breather. This motivates the study of the effect of temperature on breathers.

6.2. Models of noise

We have taken several approaches to treating noise. There is a surprising degree of subtlety here (noted by other researchers as well [63–66]). It turns out that simply adding Gaussian white noise to the initial coordinates of the atoms is unsatisfactory: either nothing happens (low noise) or the breather could *increase* its amplitude and other breathers could form spontaneously (high noise).

Better results are obtained by extending the model. In [24, 67] dissipative effects on the breather due to transverse waves, i.e. phonons representing the motion of off-chain ions, which drain the breather energy, have been explored. Generally, this involves the introduction of additional degrees of freedom. Figure 25 demonstrates how, induced by a phonon kick [24], energy radiates away. At low temperatures there are few transverse phonons that could cause the effect, but their number rises with increasing temperature. This corresponds to a weakening of the breather directly parallel to the observed temperature evolution of the decay anomaly.

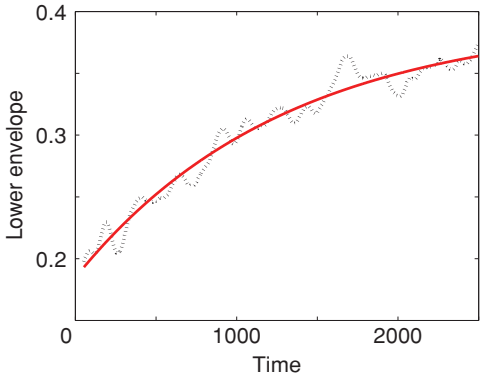

Figure 26. Time dependence of averaged minima (dots) of the oscillatory motion of the first atom of the chain. The oscillations are fit by an exponential function of the form (up to constants) $1 - \exp(-\gamma_{\text{low}} t)$; $\gamma_{\text{low}} = 7.76 \times 10^{-4}$, the level of noise is 0.35.

In [67] the finite temperature effect is simulated by modeling the transverse effects in greater dynamical detail. As before, we represent increasing temperature by increasing the Gaussian white noise added to the initial coordinates of the members of a linear chain. But although we continue to work with the one-dimensional chain, each member of the chain is given an additional degree of freedom associated with motion along a direction transverse to the chain. The idea is that in general the discrete breather phenomenon is most strongly elicited in one dimension, and that at low temperature, due to the Jahn–Teller symmetry breaking, the principal dynamical activity takes place in a single dimension. However, as temperature rises, additional degrees of freedom, and in particular transverse modes of the atoms of our chain, may have thermal excitations that allow energy to be shunted away from the pure breather modes. A higher effective dimension also affects the breather through the appearance of thresholds. In a dimension greater than 1, localization may not occur despite nonlinearity—if the nonlinearity is too weak.

To quantify the breather decay we define a parameter γ_{low} associated with the rate of lattice relaxation (breather dissipation). This parameter is calculated from the fit of the *lower envelope* of the oscillatory motion of the first atom of the chain relaxing into its new equilibrium position. The *lower envelope* refers to the sequence of averaged extrema of the oscillatory motion that are close to the impurity. This measure of lattice position reflects the expectation that the transitions induced by the non-relaxed lattice (cf [2, 17]) are most likely to occur at the times of extreme force on the quasi-molecule electronic wave function. An example of the lower envelope fit providing the parameter γ_{low} is in figure 26. We study the temperature (noise) evolution of γ_{low} to get a picture of the speed of breather decay. The wide variation in response to noise requires a study of the statistics of γ_{low} as a function of noise (the experimental data are effectively an average over such statistics). The dependence of $\gamma_{\text{low}}^{\text{A}}$ on the noise (temperature) is displayed in figure 27. The graph shows monotonic increase of the breather relaxation speed with temperature which consistently reflects the experimental observation where the decay anomaly weakens with increasing temperature and gradually fades.

6.3. Non-dissipative incoherent reflection

Reference [68] returns to simpler models. The reason is that it uses more satisfactory ways to deal with problems that arose in the pure one-dimensional model. The principal innovation is

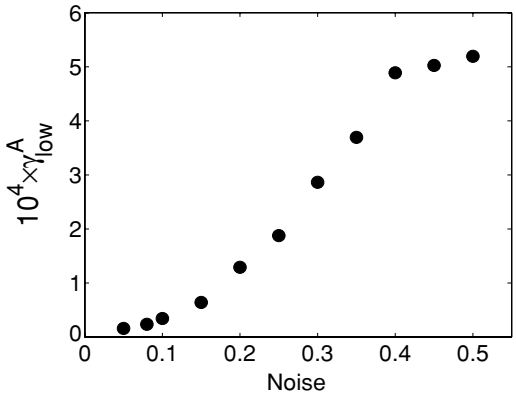

Figure 27. Noise (temperature) dependence of the γ^{A}_{low} parameter.

the introduction of *non-dissipative incoherent reflection*. Its virtue is improved modeling of the contact with the heat bath. This gives reasonable results when compared to experiment.

To create breathers at zero temperature, one generally begins with all atoms at rest and applies an intense push on the first atom, simulating the force of the distorted impurity center. This leads to reflections off the far end of the chain. Such reflections are unphysical and lead to artificial focusing, which in turn can lead to breather enhancement rather than dissipation. At zero-temperature this is not a problem, since one can put damping on the far end of the chain. However, at higher temperatures that strategy will artificially cool the system.

We have therefore developed an alternative scheme for breaking up the radiated shock wave; it is related to Anderson localization [69]. A one-dimensional system with randomness can only support localized excitations. We take advantage of this by slightly randomizing the masses at the far end of the chain. A wave impinging on them will be reflected to some extent, but in a sufficiently chaotic manner that the collective effects of the reflected wave are ameliorated.

Our procedure was to randomize the masses of about 40% of the atoms on the far end of the chain, allowing them to depart by at most 25% from the values they would otherwise have had. This maintains energy conservation, hence temperature constancy, while dissipating the shockwave (in the sense of coherence, not energy loss). A portion of the breather formation energy is added to that introduced by temperature, but this only renormalizes noise values.

The method of incoherent reflection in fact may prove useful in a variety of modeling situations where one necessarily has a finite model but nevertheless wants to simulate an infinite system. It is a way to suppress reflections off the boundary without loss of energy. In figure 28 we present a comparison of kinetic energy with and without randomization of masses.

Noise is introduced in two ways. Method 1 uses randomly distributed initial velocities for all atoms, with temperature related to noise level. Method 2 excites each mode of the system in such a way that the energy per mode follows the Boltzmann distribution for a given temperature.

As in [67], we characterize breather decay by a parameter γ_{low} associated with the speed of lattice relaxation (breather dissipation). We again studied the statistics of γ_{low} as a function of temperature/noise (the experimental data are also such an average). The higher γ_{low}, the faster the breather decay. Figure 29 displays γ^{A}_{low} as a function of temperature (or noise). Because of the limitations of the model we do not expect quantitative precision, but take the

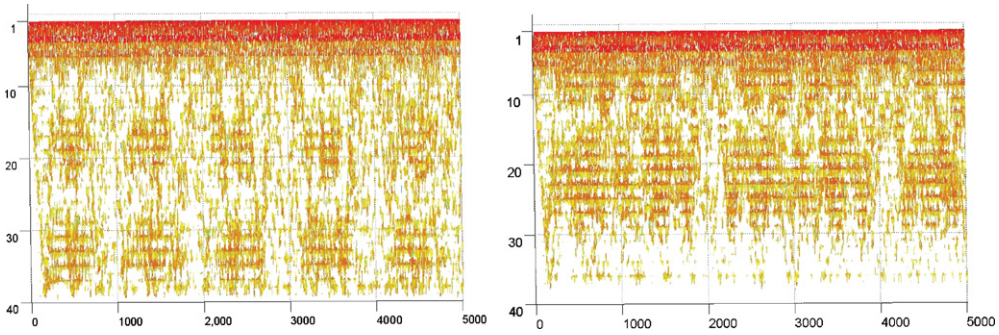

Figure 28. Kinetic energy with and without randomization of masses. Time runs horizontally. Atom number is the vertical axis, with atom 1 at the top of the figure. Where the graph is marked, the kinetic energy exceeds about 10^{-3} for that atom at that time. In the first figure one can see a periodic pattern due to the initial shock wave going out from the breather area (at the top), bouncing off the end of the chain (bottom of the figure) and continuing to echo back and forth. In the second figure masses are randomized near the end of the chain and traveling waves are not supported in this area. The reflection is less coherent and the residual energy (what is not part of the idealized breather) sloshes around in a way that reduces systematic effects. As indicated in the text, it was important to have a way to break up the shock waves while nevertheless conserving energy.

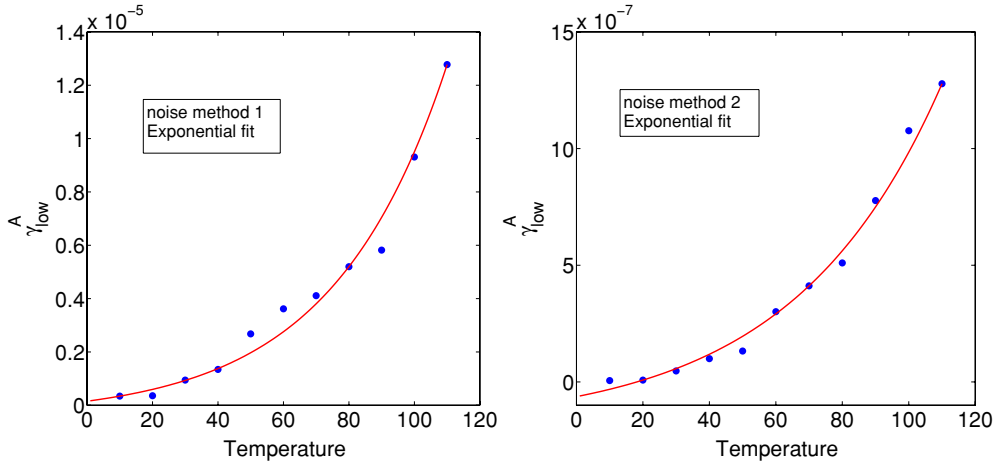

Figure 29. Temperature dependence of the average value of γ_{low} using both noise models. Noise model 1 is based on randomly distributed initial velocities. Calculated data are fit by an exponential, $5.773 \times 10^{-7} \times \exp(0.028 \times T)$. Noise model 2 is based on randomly distributed initial position and velocities. Calculated data are fit by an exponential, $1.259 \times 10^{-7} \times \exp(0.022 \times T)$.

overall monotonic increase of the breather relaxation speed with temperature as an indication thermal breather behavior is well-handled by our techniques. The increase, moreover, reflects the experimental observation that the decay anomaly weakens (and ultimately disappears) with increasing temperature.

7. Conclusions and remaining issues

The unexpected is often educational. Some anomalies in the history of physics have been of great import, for example, that occurring in the perihelion shift of mercury [70]. Others have

the potential to be. The 'Pioneer anomaly' comes to mind [71]. But the latter could turn out to be some minor forgotten and forgettable effect. Between these extremes there is room for small advances.

The work reviewed in the present article arose from an anomaly in the decay of luminescence in what should have been a well-understood system, a color center embedded in a rocksalt lattice, and which undergoes a Jahn–Teller distortion when excited. The first explanations of this anomaly posited a factor of a one billion (10^9) slowdown in crystal relaxation, which was more than some people were willing to believe. However, that slowdown can be explained once nonlinear effects in the lattice are taken into account. What happens is that a *breather* is formed, a localized oscillation, something that stays near the color center because its frequencies are outside the phonon bands—a consequence of nonlinearity.

In this article we have described our putting together the pieces of this explanation, at both the classical and the quantum levels. Although the 'educational' message is not in the league of those in our opening paragraph, nevertheless we did find ourselves bringing new ideas to the well studied Jahn–Teller effect as well as providing an experimental example of a quantum breather.

We close with a discussion of what we see as our biggest remaining challenge. Although the introduction of noise does account for the measured temperature effects in a qualitative way, one still does not have a full quantitative description. Our suspicion at this point is that there is a temperature-induced change in the matrix elements that allows the decay of the long-lived metastable level. To some extent, this is already known to exist [4], but stronger effects may be present.

Acknowledgments

We thank our co-authors and colleagues who have contributed to this work. Among them are Serge Aubry, Mauro Bacci, Vladislav Čápek, Robert Englman, Paolo Facchi, Sergej Flach, Jason Fleischer, Victor Fleurov, Bernard Gaveau, Jiří Hlinka, Karel Polák, Daniela Mugnai, Martin Nikl, Karel Nitsch, Saverio Pascazio, Phil Pechukas, Anedio Ranfagni, Antonello Scardicchio, Avi Soffer, Charalampos Skokos, Kazuo Takatsuka, Denis Tolkunov and William Williams. We have also benefitted from the following sources of support: United States National Science Foundation grants, most recently PHY 05 55313, CNR short-term mobility program at IFAC-CNR, Florence, Czech Ministry of Education grant ME 903 and Czech Institutional Research Plan (plan no AVOZ10100521).

Appendix. Simulation parameters and physical constants

The units used in our simulations are as follows:

- Angstroms for distance.
- The mass of Br is unity and the ratio 'r' is usually taken to be 2, which is the approximate Br to K mass ratio. The factor 'M' in $V(u)$ (see its definition, following equation (15)) is thus unity.
- The Debye temperature of KBr is taken to be 173 K, leading to $\omega_{\text{Debye}} \sim 2.3 \times 10^{13}$ s^{-1} and $2\pi/\omega_{\text{Debye}} \sim 0.3$ ps.
- The time unit is $1/\omega_0$, with ω_0 the frequency in $V(u)$. Thus, ω_0 also becomes unity. The relation between ω_0 and ω_{Debye} was discussed in [23] and in the present notation is given by $\omega_0 = \omega_{\text{Debye}}\sqrt{2(1+1/r)}/((6\pi^2)^{1/3})$.

In these units $\hbar$ is approximately 0.007 897, one unit of energy is about 0.839 eV and the time unit close to 0.1 ps. Note that these values are sensitive to the way in which ω_0 was fixed. If one instead sets its value by matching the bulk speed of sound in KBr, the time unit increases by a factor 1.7, with a corresponding significant decrease in the energy scale.

For the nonlinearity parameter, λ (of $V(u)$), we took the value 1. Allowing for differences in units this is in the same range that other authors have used [72]. The push from the expanded quasimolecule is expressed through the non-dynamic q_0 which was taken to be 1. With this value the equilibrium value of the Br is displaced by about 8% of the ion separation distance (which is about 3.3 Å) and the instantaneous push somewhat more.

The 'holding' parameter, ν, was often taken to be 4, reflecting the number of off-chain nearest neighbors each ion has.

For most simulations we used 30 ions, although occasionally more (and more rarely, fewer) were used. In any case, there was little change unless there were fewer than 10. Similar remarks apply to most of the other parameters above. Setting $r = 1$ yields a qualitative change, since there is no longer a gap between acoustic and optical phonons. Nevertheless, with sufficient nonlinearity there were breathers.

References

[1] Polák K, Nikl M and Mihóková E 1992 Decay kinetics of the slow component of Pb^{2+} emission in KX (X = Cl, Br, I) *J. Lumin.* **54** 189–96

[2] Gaveau B, Mihóková E, Nikl M, Polák K and Schulman L S 1998 Anomalous decay of the slow component of Pb^{2+} emission *Phys. Rev.* B **58** 6938–43

[3] Flach S and Gorbach A V 2008 Discrete breathers—advances in theory and applications *Phys. Rep.* **467** 1–116

[4] Hlinka J, Mihóková E and Nikl M 1991 Kinetics of A-luminescence in KCl:Tl. Multiphonon processes *Phys. Status Solidi* b **166** 503

[5] Hlinka J, Mihóková E, Nikl M, Polák K and Rosa J 1993 Energy transfer between A_T and A_X minima in KBr:Tl *Phys. Status Solidi* b **175** 523

[6] Mihóková E, Nikl M, Polák K and Nitsch K 1994 Decay kinetics of the 408 nm emission band from Pb^{2+} centres in KI single crystals. *J. Phys.: Condens. Matter* **6** 293

[7] Nikl M, Hlinka J, Mihóková E, Polák K, Fabeni P and Pazzi G P 1993 Decay Kinetics of CsI:Tl luminescence excited in A-absorption band *Phil. Mag.* B **67** 627

[8] Jahn H A and Teller E 1937 Stability of polyatomic molecules in degenerate electronic states: I. Orbital degeneracy *Proc. R. Soc.* A **161** 220–35

[9] Jahn H A 1938 Stability of polyatomic molecules in degenerate electronic states: II. Spin degeneracy *Proc. R. Soc.* A **164** 117–31

[10] Jacobs P W M 1991 Alkali halide crystals containing impurity ions with the ns^2 ground-state electronic configuration *J. Phys. Chem. Solids* **52** 35–67

[11] Hiznyakov V V and Kristoffel N N 1984 *The Dynamical Jahn–Teller Effect in Localized Systems* (Amsterdam: Elsevier)

[12] Kang J G, Cusso F, Belliveau T F and Simkin D J 1985 Emission spectra and decay kinetics of the A-band emission from Pb^{2+} centres in KCl and KI single crystals *J. Phys. C: Solid State Phys.* **18** 4753–65

[13] Gaveau B, Mihóková E, Nikl M, Polák K and Schulman L S 2001 Anomalous decay of the slow component in doped alkali halides *J. Lumin.* **92** 311–6

[14] Evans R C 1983 *An Introduction to Crystal Chemistry* (Cambridge: Cambridge University Press)

[15] Mihóková E, Schulman L S, Nikl M, Polák K and Gaveau B 2002 Temperature dependence of anomalous decay: theory and experiment. *Phys. Rev.* B **66** 155102

[16] Loudon R 1946 *The Quantum Theory of Light* 2nd edn (Oxford: Clarendon)

[17] Schulman L S, Scardicchio E M A, Facchi P, Nikl M, Polák K and Gaveau B 2002 Slow relaxation, confinement and solitons *Phys. Rev. Lett.* **88** 224101

[18] Takatsuka K 1992 Extraction of accurate frequencies from fast fourier transform spectra *J. Comput. Phys.* **102** 374–80

[19] Lichtenberg A J and Lieberman M A 1983 *Regular and Stochastic Motion* (New York: Springer)

[20] Arnold V I 1978 *Mathematical Methods of Classical Mechanics* (New York: Springer)

[21] Mihóková E, Schulman L S, Polák K and Williams W 2004 The role of breathers in anomalous decay *Phys. Rev.* E **70** 016610

[22] Kiselev S A, Bickham S R and Sievers A J 1994 Anharmonic gap mode in a one-dimensional diatomic lattice with nearest-neighbor Born–Mayer–Coloumb potentials and its interaction with a mass-defect impurity *Phys. Rev.* B **50** 9135–52

[23] Schulman L S 2003 Semiclassical quantization of localized lattice solitons *Phys. Rev.* A **68** 052109

[24] Schulman L S, Mihóková E and Polák K 2006a Anomalous decay and breather formation in doped alkali halides *J. Lumin.* **121** 465–9

[25] MacKay R S and Aubry S 1994 Proof of existence of breathers for time-reversible or Hamiltonian networks of weakly coupled oscillators *Nonlinearity* **7** 1623–43

[26] Campbell D K, Flach S and Kivshar Y S 2004 Localizing energy through nonlinearity and discreteness *Phys. Today* **57** 43–9

[27] Schulman L S and Mihóková E 2008 Torus doubling resonances and breather stability *Phys. Rev.* E **78** 026212

[28] Thompson J M T and Stewart H B 1986 *Nonlinear Dynamics and Chaos: Geometrical Methods for Engineers and Scientists* (Chichester: Wiley)

[29] Barger V D and Olsson M G 1995 *Classical Mechanics: A Modern Perspective* 2nd edn (New York: McGraw-Hill)

[30] Wilczak D and Zgliczynski P 2007 Period doubling in the Rossler system—a computer assisted proof arXiv:0712.1123v1

[31] Einstein A 1917 Zum Quantensatz von Sommerfeld und Epstein *Verh. Deutsch. Phys. Ges.* **19** 82–92

[32] Brillouin L 1926 Remarques sur la mécanique ondulatoire *J. Phys. Radium* **7** 353–68

[33] Keller J B 1958 Corrected Bohr–Sommerfeld quantum conditions for nonseparable systems *Ann. Phys.* **4** 180–8

[34] Eastes W and Marcus R A 1974 Semiclassical calculation of bound states in a multidimensional system *J. Chem. Phys.* **61** 4301–6

[35] Noid D W and Marcus R A 1975 Semiclassical calculation of bound states in a multidimensional system. Use of Poincaré's surface of section *J. Chem. Phys.* **62** 2119–24

[36] Noid D W, Koszykowski M L and Marcus R A 1977 A spectral method of obtaining molecular spectra from classical trajectories *J. Chem. Phys.* **67** 404–7

[37] Noid D W and Marcus R A 1977 Semiclassical calculation of bound states in a multidimensional system for nearly 1:1 degenerate systems *J. Chem. Phys.* **67** 559–67

[38] Sohlberg K, Tuzun R E, Sumpter B G and Noid D W 1998 Full three-body primitive semiclassical treatment of H_2^+ *Phys. Rev.* A **57** 906–13

[39] Percival I C 1977 Semiclassical theory of bound states *Advances in Chemical Physics* ed I Prigogine and S A Rice (New York: Wiley Interscience)

[40] Martens C C and Ezra G S 1985 EBK quantization of nonseparable systems: a Fourier transform method *J. Chem. Phys.* **83** 2990–3001

[41] Martens C C and Ezra G S 1987a Classical and semiclassical mechanics of strongly resonant systems: a Fourier transform approach *J. Chem. Phys.* **86** 279–307

[42] Martens C C and Ezra G S 1987b Classical, quantum mechanical, and semiclassical representations of resonant dynamics: a unified treatment *J. Chem. Phys.* **87** 284–302

[43] Ezra G S, Richter K, Tanner G and Wintgen D 1991 Semiclassical cycle expansion for the helium atom *J. Phys. B: At. Mol. Opt. Phys.* **24** L413–20

[44] Schulman L S 1971 Approximate topologies *J. Math. Phys.* **12** 304–8

[45] Schulman L S 2005 *Techniques and Applications of Path Integration* (New York: Dover) with supplements

[46] Laskar J 1999 Introduction to frequency map analysis *Hamiltonian Systems with Three or More Degrees of Freedom: Proc. NATO Advanced Study Institute 3DHAM95* (S'Agaro, June 1995) pp 134–50

[47] Schulman L S 1968 A path integral for spin *Phys. Rev.* **176** 1558–69

[48] Karo A M and Hardy J R 1963 Lattice dynamics and specific-heat data for Rocksalt-Structure alkali halides *Phys. Rev.* **129** 2024–36

[49] Flach S and Willis C R 1998 Discrete breathers *Phys. Rep.* **295** 182–264

[50] Wang W Z, Gammel J T, Bishop A R and Salkola M I 1996 Quantum breathers in a nonlinear lattice *Phys. Rev. Lett.* **76** 3598–601

[51] Fleurov V, Schilling R and Flach S 1998 Tunneling of a quantum breather in a one-dimensional chain *Phys. Rev.* E **58** 339–46

[52] Flach S, Fleurov V and Ovchinnikov A A 2001 Tunneling of localized excitations: giant enhancement due to fluctuations *Phys. Rev.* B **63** 094304 (9 pp)

[53] Konotop V V and Takeno S 2001 On quantization of weakly nonlinear lattices. Envelope solitons *Phys. Rev.* E **63** 066606

[54] Hizhnyakov V 1996 *Phys. Rev.* B **53** 13981
Hizhnyakov V 1999 *Europhys. Lett.* **45** 508
Hizhnyakov V and Nevedrov A 1997 *Phys. Rev.* B **56** R2908
Hizhnyakov V, Nevedrov A and Sievers A J 2002 *Physica* B **316–317** 132
[55] Flach S, Fleurov V and Gorbach A V 2005 Classical and quantum radiation of perturbed discrete breathers *Phys. Rev.* B **71** 064302
[56] Schulman L S, Tolkunov D and Mihóková E 2006 Stability of quantum breathers *Phys. Rev. Lett.* **96** 065501
[57] Schulman L S, Tolkunov D and Mihóková E 2006b Structure and time-dependence of quantum breathers *J. Chem. Phys.* **322** 55–74
[58] Feynman R P and Hibbs A R 1965 *Quantum Mechanics and Path Integrals* (New York: McGraw-Hill)
[59] Feynman R P 1955 Slow electrons in a polar crystal *Phys. Rev.* **97** 660
[60] Feynman R P 1972 *Statistical Mechanics: A Set of Lectures* (Reading, MA: Benjamin)
[61] Weiss U 1999 *Quantum Dissipative Systems* 2nd edn (Singapore: World Scientific)
[62] Schulman L S 1974 Some differential-difference equations containing both advance and retardation *J. Math. Phys.* **15** 295–8
[63] Reigada R, Sarmiento A and Lindenberg K 2001 Energy relaxation in nonlinear one-dimensional lattices *Phys. Rev.* E **64** 066608
[64] Reigada R, Sarmiento A and Lindenberg K 2002a Energy relaxation in Fermi–Pasta–Ulam arrays *Physica* A **305** 467–85
[65] Reigada R, Sarmiento A and Lindenberg K 2002b Asymptotic dynamics of breathers in Fermi–Pasta–Ulam chains *Phys. Rev.* E **66** 046607
[66] Reigada R, Sarmiento A and Lindenberg K 2003 Breathers and thermal relaxation in Fermi–Pasta–Ulam arrays *Chaos* **13** 646–56
[67] Schulman L S and Mihóková E 2006 Model of temperature-dependent crystal relaxation *Phys. Status Solidi* c **3** 3430–3
[68] Mihóková E and Schulman L S 2009 Noisy breathers and temperature-dependent luminescence decay *J. Lumin.* **129** 1878–81
[69] Anderson P W 1958 Absence of diffusion in certain random lattices *Phys. Rev.* **109** 1492–505
[70] Einstein A 1916 Die Grundlage der allgemeinen Relativitätstheorie *Ann. Phys., Lpz.* **49** 769–822
[71] Nieto M M and Anderson J D 2007 Search for a solution of the pioneer anomaly *Contemp. Phys.* **48** 41–54
[72] Bickham S R and Sievers A J 1991 Intrinsic localized modes in a monatomic lattice with weakly anharmonic nearest-neighbor force constants *Phys. Rev.* B **43** 2339–46
[73] Ranfagni A, Mugnai D, Fabeni P and Pazzi G P 2002 Statistical-dynamical validity of a Jahn–Teller model for Tl^+ luminescence *Phys. Rev.* B **66** 184107